



CHEMISTRY

Modification of ground-state chemical reactivity via light-matter coherence in infrared cavities

Wonmi Ahn¹, Johan F. Triana², Felipe Recabal², Felipe Herrera^{2,3*}, Blake S. Simpkins^{4*}

Reaction-rate modifications for chemical processes due to strong coupling between reactant molecular vibrations and the cavity vacuum have been reported; however, no currently accepted mechanisms explain these observations. In this work, reaction-rate constants were extracted from evolving cavity transmission spectra, revealing resonant suppression of the intracavity reaction rate for alcoholysis of phenyl isocyanate with cyclohexanol. We observed up to an 80% suppression of the rate by tuning cavity modes to be resonant with the reactant isocyanate (NCO) stretch, the product carbonyl (CO) stretch, and cooperative reactant-solvent modes (CH). These results were interpreted using an open quantum system model that predicted resonant modifications of the vibrational distribution of reactants from canonical statistics as a result of light-matter quantum coherences, suggesting links to explore between chemistry and quantum science.

Controlling chemical reactions with electromagnetic fields is a long-standing goal in chemistry and physics (1, 2). Femtosecond laser pulses can transiently excite vibrational modes of reactant molecules to selectively promote breaking or forming of chemical bonds (3–5). However, fast energy redistribution in polyatomic molecules severely limits this approach, despite efforts to overcome this obstacle using laser pulse shaping (6, 7).

Chemical control without lasers has been recently demonstrated using cavities (8–12). In this approach, hybrid light-matter polariton states arise from strong interactions of dipole-allowed molecular transitions with the cavity vacuum at optical (13) and infrared frequencies (14–16). Experiments show inhibition of excited-state processes such as photoisomerization (17) and photobleaching (18) in visible cavities and also modification of bond formation and cleavage rates in infrared cavities as a result of vibrational strong coupling (VSC) (8–10, 19). VSC is characterized by collective molecular response in transmission (20, 21), a spatial dependence of the interaction that follows the mode profile (22, 23), and reversible modulation of the system using ultrafast lasers (24, 25) or electrochemistry (26, 27).

Achieving coupling-induced selective chemistry would enable chemical catalysis by design, but challenges to its reproducibility (28, 29) and lack of mechanistic explanation have stifled progress. Here, we report robust experimental evidence of cavity-modified chemistry and describe a theory consistent with measurements.

We studied the alcoholysis of phenyl isocyanate (PHI) with cyclohexanol (CHol) in tetrahydrofuran (THF) to give urethane [cyclohexyl carbamate (CC)]. The reaction is exothermal (30), has a low activation energy (31), and resonant cavity modes can be tuned to reactant, product, or solvent vibrational modes. We measured a strong cavity-tuning dependence of the reaction kinetics, with rate constants reduced by 30 to 80%, and developed a quantum model that qualitatively agrees with observations and provides mechanistic understanding for intracavity reaction kinetics. Our theory proposes that the intracavity reactivity depends on stationary light-matter coherences, and we discuss the importance of energy disorder in preserving coherence over chemical time scales.

Results and discussion

The alcoholysis of isocyanates is well understood (31–33) and proceeds through concerted nucleophilic addition at the NC bond in isocyanate (31, 33, 34). The geometry of the PHI-CHol complex (Fig. 1A) involves an NHO hydrogen bond that evolves into a cyclic NHOC structure in the transition state (3). Cleavage of the HO bond results in ring opening and exothermic formation of urethane ($\Delta H_{rxn} \approx -20.5$ kcal/mol) with activation energy of 6.7 kcal/mol (2343 cm⁻¹) in THF. The second-order rate constant at room temperature is $k_0 = 0.59 \times 10^{-5}$ M⁻¹·s⁻¹ (3). Back reactions are negligible.

We injected the reactant solution into a thin-layer cell bounded by transparent CaF₂ windows, for out-of-cavity control measurements, or by Au-coated CaF₂ windows, for cavity-coupled measurements [Fig. 1B; additional details in section 1 of the supplementary materials (SM)]. Figure 1C shows two sets of transmission spectra. For control measurements (upper curves, red), reactant bands decreased (NCO stretch of PHI at ~2260 cm⁻¹ and OH band of CHol at ~3470 cm⁻¹), and

product bands grew (CO at 1730 cm⁻¹ and at 3293 cm⁻¹; see detailed spectra in figs. S1–S2). The NCO band absorption was converted to reactant concentration through direct proportionality (see procedure in section 1 of the SM and fig. S3 for extinction coefficient calibration), then inverted and plotted against time (Fig. 1D), yielding a line whose slope equaled the second-order rate constant (35). The average of six such measurements gave a control rate constant $k_0 = (2.34 \pm 0.2) \times 10^{-5}$ M⁻¹·s⁻¹ (datasets in fig. S4). This rate was higher than in previous reports (32), which involved lower reactant concentrations. The rates measured under our conditions were consistent in independent measurements performed in a period of 24 months, with all reactions (control and cavity-coupled) carried out using the same initial reactant concentrations.

Typical transmission spectra for a cavity-coupled sample are shown in Fig. 1C (lower curves, blue). These example data exhibited multiple resonant peaks, with one coupled to the NCO band of PHI (2260 cm⁻¹), giving a splitting at normal incidence of 112 cm⁻¹ (cavity $Q \sim 100$, cavity linewidth $\kappa \approx 38$ cm⁻¹; see table S2). These evolving transmission spectra were fit to a function that accounted for the absorbance of the intracavity medium (Fig. 1E), which, again, was directly proportional to reactant concentration. We inverted and plotted this data (Fig. 1F) to extract a rate constant $k = (1.48 \pm 0.2) \times 10^{-5}$ M⁻¹·s⁻¹ for this sample, ~37% lower than uncoupled controls. Collection of the entire cavity dispersion allowed identification and fitting of spectra showing strong interaction with the mode of interest regardless of tuning at normal incidence [see the model in section 3.3 of the SM and (14, 21, 23, 25, 27)].

Reaction rates were extracted for different cavities. The resulting “action spectrum” (9) is shown in Fig. 2A. The initial (blue) and final (orange) transmission spectra of the control solution are shown to identify relevant vibrational modes. There was a strong dependence of the reaction rate on the cavity mode tuning, with rate suppression due to VSC on reactant (NCO), product (CO), and cooperative reactant-solvent (CH) modes (full dataset in fig. S8 and table S1). Cavity-induced suppression spanned 30 to 80%, relative to uncoupled controls. The largest suppression was found for cavities tuned to the NCO reactant mode, with a frequency dependence that closely followed the shape of the NCO absorption band. The rate constants for far-detuned cavities (squares) were close to the out-of-cavity rates ($k/k_0 \sim 0.91$; see table S1). Figure 2B shows representative inverse concentration plots and linear fits for cavities tuned to the reactant NCO and reactant-solvent CH bands, highlighting the lower slopes (rates), relative to out-of-cavity controls. Our mechanistic discussion below

¹UNAM – National Nanotechnology Research Center and Institute of Materials Science and Nanotechnology, Bilkent University, Ankara, Turkey. ²Department of Physics, Universidad de Santiago de Chile, Santiago, Chile. ³Millennium Institute for Research in Optics (MIRO), Concepción, Chile. ⁴Chemistry Division, US Naval Research Laboratory, Washington, DC, USA.
*Corresponding author. Email: blake.simpkins@nrl.navy.mil (B.S.S.); felipe.herrera.u@usach.cl (F.H.)

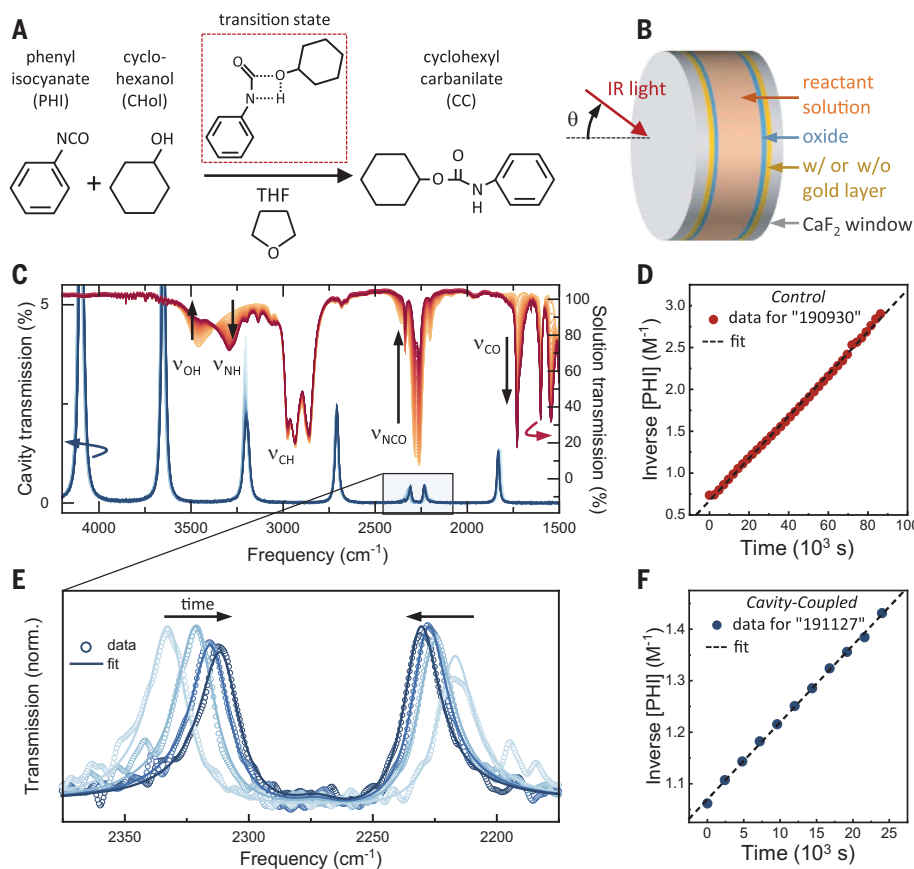


Fig. 1. Description of urethane monomer formation and reaction monitoring. (A) The reactants phenyl isocyanate (PHI) and cyclohexanol (CHol) were combined in tetrahydrofuran (THF) to form cyclohexyl carbamate (CC). (B) Solution was contained between two CaF_2 windows that were either transparent (for control measurements) or coated with Au/SiO_2 (for cavity-coupled experiments). (C) Time-dependent Fourier transform infrared transmission spectra for out-of-cavity control measurements (red hues) showed reactant absorptions, v_{NCO} of PHI at 2260 cm^{-1} and v_{OH} of CHol at 3470 cm^{-1} , diminished as the reaction proceeded, while product features, v_{CO} at 1730 cm^{-1} and v_{NH} at 3293 cm^{-1} , increased. The v_{NCO} absorption was converted to PHI concentration, inverted, and plotted versus time to extract the second-order reaction rate constant as shown in (D). The blue curves in (C) correspond to a time series of cavity-coupled transmission spectra showing strong coupling between the cavity and NCO vibrational mode of the PHI reactant. These spectra were fit, as shown in (E), to yield time-dependent PHI concentration, which was inverted, plotted, and fit to yield the reaction rate constant under cavity-coupled conditions. One typical cavity-coupled dataset is shown in (F).

focuses on the NCO band because it plays a prominent role in the reaction, however, modification of one mode can influence others (intramolecular vibrational relaxation, Fermi coupling, etc.). Further, we note that the product-coupled cavity also supported a higher-order mode that weakly coupled to the reactant OH mode ($\sim 3500\text{ cm}^{-1}$), however, we have only highlighted modes under strong coupling. The role of weak coupling in chemical reactivity has yet to be fully understood.

Our mechanistic description of VSC-modified reactivity started by modeling the vibrational structure of the PHI molecule in the frequency region of the NCO band, which includes a fundamental NCO stretch, v_6 , and a Fermi resonance between v_6 and a combination of

low-frequency CH bending modes (analysis in section 4 of the SM). The NCO fundamental at 2260 cm^{-1} was inhomogeneously broadened (full width at half maximum $\approx 47\text{ cm}^{-1}$; see fig. S13). We modeled an ensemble of N reactant NCO vibrations under VSC at 300 K , considering vibrational relaxation, cavity decay, thermalization, and many-body correlations, using an open quantum system approach (see sections 5 and 6 of the SM). Field-dependent dipole self-energy terms (36) were not included. The theory suggested that although the coupled vibration-cavity system was at thermal equilibrium with its environment, as confirmed by experiments (37), when tracing out the photonic degrees of freedom, the stationary vibrational population of reactants could deviate

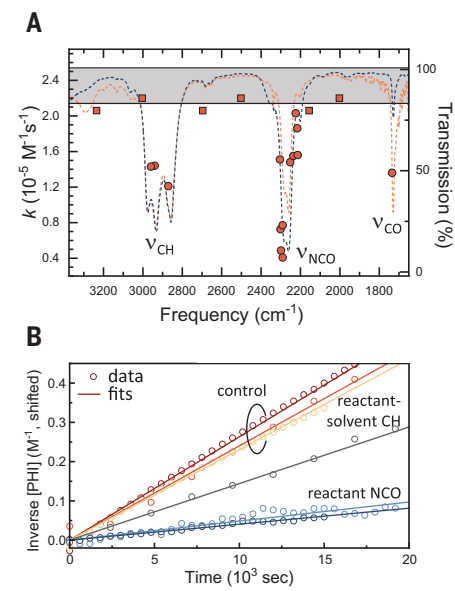


Fig. 2. Cavity-modified chemical reactivity.

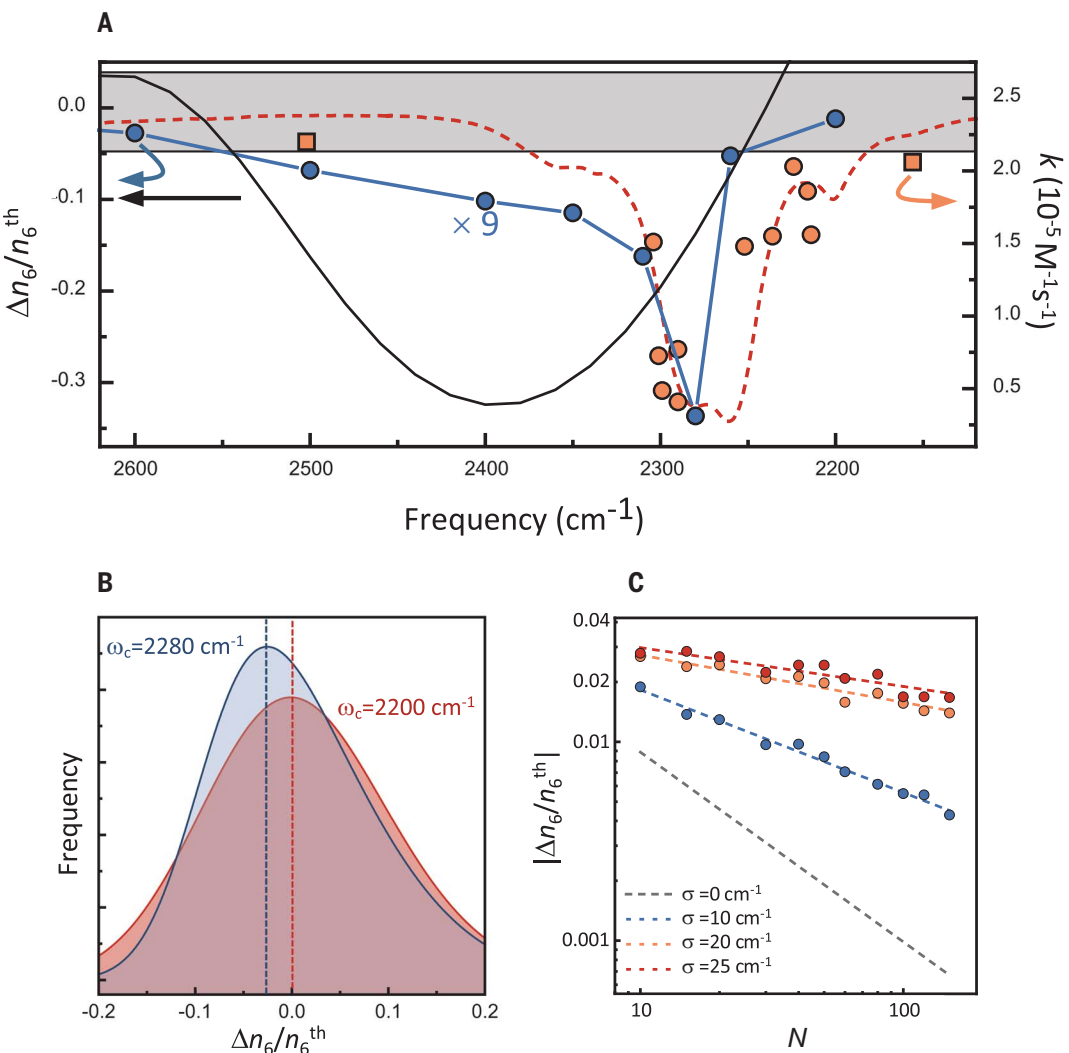
The action spectrum presented in (A) shows the extracted reaction rate constants (orange symbols) as a function of cavity tuning (i.e., Fabry-Perot mode position at normal incidence). The gray horizontal band represents the average out-of-cavity control rate with its width equal to the standard deviation of six measurements. Blue and orange dashed curves correspond, respectively, to initial and final transmission spectra. Reaction suppression was observed when the cavity was tuned to prominent vibrational modes. Several example linear fits, from which reaction rate constants were extracted, are shown in (B).

from canonical Boltzmann statistics. This phenomenon has been shown to occur for other strongly coupled subsystems (38), but its potential consequences in cavity chemistry have yet to be fully explored. In this picture, chemical bonds can break and form through local two-body processes with the vibrational level statistics modified by the strongly interacting photonic environment. This insight can be complemented by other approaches wherein the cavity photon quadrature is treated as another classical coordinate that contributes to a static polaritonic potential energy surface (39, 40).

In Fig. 3A, we show the deviation of the most-probable v_6 occupation from its cavity-free canonical Boltzmann value, $\Delta n_6/n_6^{\text{th}}$, as a function of cavity frequency, for an ensemble of PHI molecules ($N = 50$) with a Gaussian distribution of v_6 mode frequencies (variance = σ^2), coupled to a single cavity mode. Cavity-modified rate measurements (orange points reproduced from Fig. 2A) and the PHI transmission spectrum (orange dashed curve) are also shown. This single-mode theory predicted a narrow vibrational depopulation feature (blue

Fig. 3. Comparison of cavity-modified reactivity with theoretical prediction.

(A) The NCO region of the action spectrum of Fig. 2 is reproduced here. Single-mode theory predicted a resonant depopulation of the v_6 mode (blue points) that qualitatively followed the experimental data well. Example cavity-induced population redistribution is shown in (B). A multimode single-molecule treatment, solid black curve in (A), yielded a resonant depopulation effect that was considerably stronger in magnitude (note the 9 \times scaling applied to the single-mode analysis) but was broader and blue-shifted relative to the experimental results. Although the cavity-induced effect was predicted to diminish with increased oscillator number, N , the scaling power strongly depended on molecular disorder (C). Molecular disorder, σ , was defined as a Gaussian broadening of the Lorentzian linewidth.



circles, $\Delta n_6/n_6^{\text{th}} < 0$) which closely followed the transmission lineshape and was most prominent at the frequency of the combination band (2280 cm^{-1}), in qualitative agreement with the measured action spectrum. Figure 3B shows that at large detuning, the vibrational occupation of v_6 was symmetrically centered at the canonical Boltzmann average, but near-resonant cavities gave a skewed distribution of $\Delta n_6/n_6^{\text{th}}$, whose most-probable value corresponded to net vibrational depopulation (additional histograms in fig. S14). The formal connection between $\Delta n_6/n_6^{\text{th}}$ and the reaction rate has yet to be developed (see ansatz in section 6 in the SM).

The single-mode many-particle analysis qualitatively agreed with the experimental data and improved our understanding of cavity-suppressed reactivity. However, the predicted values of $\Delta n_6/n_6^{\text{th}}$ were relatively small. This result was due to the many-particle model not accounting for the full dispersion of the cavity field. Treating large N and a continuum of cavity modes is prohibitive, but we could gain insight

by treating a single PHI molecule in a multimode Fabry-Perot cavity with a quasi-continuous spectrum ω_k , where k denotes the in-plane wave number (details in section 6.2 of the SM). We showed that $\Delta n_6/n_6^{\text{th}}$ in this case is proportional to $\sum_k (g_{6,k}/\gamma_6) \text{Im} \langle \hat{a}_k \hat{b}_6^\dagger \rangle_{\text{ss}}$, where $\langle \hat{a}_k \hat{b}_6^\dagger \rangle_{\text{ss}}$ is the stationary light-matter coherence between the vibrational mode and the k th cavity mode, $g_{6,k}$ is the Rabi frequency, and γ_6 is the homogeneous vibrational linewidth. Solving for the steady-state coherence gave

$$\Delta n_6/n_6^{\text{th}} = \sum_k P(\omega_k) \left(e^{-\Delta_{k,6}/k_B T} - 1 \right) \quad (1)$$

where $\Delta_{k,6} = \omega_k - \omega_{v_6}$ is the detuning of v_6 from the k th mode, and $P(\omega_k)$ is a normalized distribution function scaling with $(g_{6,k}/\Delta_{k,6})^2$ for $|\Delta_{k,6}| \gg \gamma_6$. Figure 3A (solid black curve) shows that the frequency response from Eq. 1 was much broader and blue-shifted relative to experiments. However, integrating over the cavity dispersion gave values of $\Delta n_6/n_6^{\text{th}}$ considerably

larger than the single cavity mode approach, suggesting that the entire photon spectrum contributed to cavity chemistry phenomena.

Finally, we addressed the N -scaling of the vibrational depopulation effect. Because the total vibration-cavity system was in thermal equilibrium (37), deviation of the photonic occupation from a canonical distribution by δn would correspond to a redistribution of vibrational occupation per molecule of $-\delta n/N$. Therefore, for typical values of $N \sim 10^6$ in Fabry-Perot cavities, the population redistribution on individual molecules should be negligible. However, in Fig. 3C we showed that this many-body dilution behavior did not hold in general for ensembles with frequency disorder, by plotting $\Delta n_6/n_6^{\text{th}}$ as a function of N for different values of the disorder width σ (see also fig. S15). We found that inhomogeneous broadening could protect resonant population redistribution from the homogeneous $1/N$ scaling, possibly due to partial delocalization of molecular states (41, 42).

Conclusions

In this work, we suppressed a ground-state addition reaction through strong coupling between molecular vibrational modes and cavity vacuum fields. This suppression reached 80%, and we found a strong cavity frequency dependence that closely followed the reactant infrared absorption spectrum. The strongest effect was for cavities resonant with an NCO mode that participated in the transition state of the reaction. We described the mechanism quantum mechanically as the emergence of stationary noncanonical vibrational populations as a result of strong vibration–cavity coupling but noted that the composite vibration–cavity polaritonic state remained in a Boltzmann thermal state. Deviations of the vibrational occupations from canonical statistics were due to stationary light–matter coherences that depended on the details of the cavity spectrum and dispersion. For molecular ensembles, we showed evidence that inhomogeneous spectral broadening could protect the light–matter coherences that influenced vibrational reactivity, suggesting fundamental links between chemistry and quantum science that have yet to be fully developed.

REFERENCES AND NOTES

1. A. H. Zewail, *Phys. Today* **33**, 27–33 (1980).
2. W. S. Warren, H. Rabitz, M. Dahleh, *Science* **259**, 1581–1589 (1993).
3. T. Stensitzki et al., *Nat. Chem.* **10**, 126–131 (2018).
4. M. Delor et al., *Science* **346**, 1492–1495 (2014).
5. Z. Lin et al., *J. Am. Chem. Soc.* **131**, 18060–18062 (2009).
6. A. Assion et al., *Science* **282**, 919–922 (1998).
7. M. P. A. Branderhorst et al., *Science* **320**, 638–643 (2008).
8. A. Thomas et al., *Angew. Chem. Int. Ed.* **55**, 11462–11466 (2016).
9. A. Thomas et al., *Science* **363**, 615–619 (2019).
10. F. J. Garcia-Vidal, C. Ciuti, T. W. Ebbesen, *Science* **373**, eabd0336 (2021).
11. B. S. Simpkins, A. D. Dunkelberger, J. C. Owrusky, *J. Phys. Chem. C* **125**, 19081–19087 (2021).
12. F. Herrera, J. Owrusky, *J. Chem. Phys.* **152**, 100902 (2020).
13. G. Khitrova, H. M. Gibbs, M. Kira, S. W. Koch, A. Scherer, *Nat. Phys.* **2**, 81–90 (2006).
14. J. P. Long, B. S. Simpkins, *ACS Photonics* **2**, 130–136 (2015).
15. A. Shalabney et al., *Nat. Commun.* **6**, 5981 (2015).
16. J. Del Pino, J. Feist, F. J. Garcia-Vidal, *New J. Phys.* **17**, 053040 (2015).
17. J. A. Hutchison, T. Schwartz, C. Genet, E. Devaux, T. W. Ebbesen, *Angew. Chem. Int. Ed.* **51**, 1592–1596 (2012).
18. B. Munkhbat, M. Wersäll, D. G. Baranov, T. J. Antosiewicz, T. Shegai, *Sci. Adv.* **4**, eaas9552 (2018).
19. J. Lather, P. Bhatt, A. Thomas, T. W. Ebbesen, J. George, *Angew. Chem. Int. Ed.* **58**, 10635–10638 (2019).
20. B. S. Simpkins et al., *ACS Photonics* **2**, 1460–1467 (2015).
21. C. Weisbuch, M. Nishioka, A. Ishikawa, Y. Arakawa, *Phys. Rev. Lett.* **69**, 3314–3317 (1992).
22. W. Ahn, I. Vurgaftman, A. D. Dunkelberger, J. C. Owrusky, B. S. Simpkins, *ACS Photonics* **5**, 158–166 (2018).
23. S. Wang et al., *J. Phys. Chem. Lett.* **5**, 1433–1439 (2014).
24. A. D. Dunkelberger et al., *ACS Photonics* **6**, 2719–2725 (2019).
25. R. Houdré et al., *Phys. Rev. B* **52**, 7810–7813 (1995).
26. J. J. Pietron, K. P. Fears, J. C. Owrusky, B. S. Simpkins, *ACS Photonics* **7**, 165–173 (2020).
27. W. Ahn, B. S. Simpkins, *APL Photonics* **5**, 076107 (2020).
28. M. V. Imperatore, J. B. Asbury, N. C. Giebink, *J. Chem. Phys.* **154**, 191103 (2021).
29. G. D. Wiesehan, W. Xiong, *J. Chem. Phys.* **155**, 241103 (2021).
30. E. Delebecq, J.-P. Pascault, B. Boutevin, F. Ganachaud, *Chem. Rev.* **113**, 80–118 (2013).
31. F. Kössl, M. Lisaj, V. Kozich, K. Heyne, O. Kühn, *Chem. Phys. Lett.* **621**, 41–45 (2015).
32. G. Raspoet, M. T. Nguyen, M. McGarragh, A. F. Hegarty, *J. Org. Chem.* **63**, 6878–6885 (1998).
33. A. A. Caraculacu, S. Coseri, *Prog. Polym. Sci.* **26**, 799–851 (2001).
34. M. Çoban, F. A. S. Konuklar, *Comput. Theor. Chem.* **963**, 168–175 (2011).
35. K. J. Laidler, *Chemical Kinetics* (Pearson Education Inc., 1987).
36. C. Schäfer, M. Ruggenthaler, A. Rubio, *Phys. Rev. A* **98**, 043801 (2018).
37. M. Seidel et al., *ACS Photonics* **6**, 1823–1825 (2019).
38. D. Xu, J. Cao, *Front. Phys. (Beijing)* **11**, 110308 (2016).
39. T. E. Li, J. E. Subotnik, A. Nitzan, *Proc. Natl. Acad. Sci. U.S.A.* **117**, 18324–18331 (2020).
40. C. Schäfer, J. Flick, E. Ronca, P. Narang, A. Rubio, *Nat. Commun.* **13**, 7817 (2022).
41. D. Wellnitz, G. Pupillo, J. Schachenmayer, *Commun. Phys.* **5**, 120 (2022).
42. M. Du, J. Yuen-Zhou, *Phys. Rev. Lett.* **128**, 096001 (2022).
43. J. F. Triana, F. Recabal, F. Herrera, B. S. Simpkins, W. Ahn, Data: Modification of ground state chemical reactivity via light–matter coherence in infrared cavities, version 2, Zenodo (2023); <https://doi.org/10.5281/zenodo.7915873>.

ACKNOWLEDGMENTS

We thank J. Owrusky, A. Dunkelberger, I. Vurgaftman, and J. Schachenmayer for discussions. **Funding:** This work was supported by US Naval Research Laboratory Nanoscience Institute, grant WU 1J03 (W.A. and B.S.S.); ANID Fondecyt Regular grant 1221420 (F.H.); ANID Fondecyt Doctorado grant 21221970 (F.R.); ANID Fondecyt Iniciación grant 11230679 (J.T.); Millennium Science Initiative Program grant ICN17_012 (F.H. and J.T.); and Programa de Cooperación Científica ECOS-ANID ECOS grant 200028 (F.H.). **Author contributions:** Conceptualization: B.S.S. and F.H. Methodology: B.S.S., F.H., and W.A. Investigation: W.A., J.T., F.R., F.H., and B.S.S. Visualization: B.S.S., J.F.T., and F.R. Funding acquisition: B.S.S. and F.H. Writing – original draft: W.A. and B.S.S. Writing – review & editing: B.S.S. and F.H.

Competing interests: None declared. **Data and materials availability:** All data needed to support the conclusions of the main text and supplementary materials have been uploaded to Zenodo (43). **License information:** Copyright © 2023 the authors, some rights reserved; exclusive licensee American Association for the Advancement of Science. No claim to original US government works. <https://www.science.org/about/science-licenses-journal-article-reuse>

SUPPLEMENTARY MATERIALS

science.org/doi/10.1126/science.ade7147

Materials and Methods

Supplementary Text

Figs. S1 to S19

Tables S1 to S4

References (44–77)

Submitted 2 September 2022; resubmitted 7 March 2023

Accepted 12 May 2023

10.1126/science.ade7147

Modification of ground-state chemical reactivity via light-matter coherence in infrared cavities

Wonmi Ahn, Johan F. Triana, Felipe Recabal, Felipe Herrera, and Blake S. Simpkins

Science, 380 (6650), .
DOI: 10.1126/science.ade7147

Editor's summary

Hybrid light-matter states called polaritons, which are formed by strong interactions between resonant molecular transitions and photonic modes in microcavities, could be used to control chemical reactions with electromagnetic fields, a long-standing goal in chemistry. Unfortunately, such “polariton chemistry” still lacks a series of convincing demonstrations. Ahn *et al.* performed a joint experimental and theoretical study of alcoholysis of phenyl isocyanate with cyclohexanol under various strong light-matter coupling conditions. Through a rigorous analysis of their theoretical and experimental results, the authors provide compelling arguments for how cavity-altered reactivity may arise. These results are needed in this emerging field because they provide an important corroboration of earlier observations that became controversial after several reports of failed attempts. —Yury Suleymanov

View the article online

<https://www.science.org/doi/10.1126/science.ade7147>

Permissions

<https://www.science.org/help/reprints-and-permissions>

Supplementary Materials for

Modification of ground-state chemical reactivity via light–matter coherence in infrared cavities

Wonmi Ahn *et al.*

Corresponding authors: Felipe Herrera, felipe.herrera.u@usach.cl; Blake S. Simpkins, blake.simpkins@nrl.navy.mil

Science **380**, 1165 (2023)
DOI: 10.1126/science.ade7147

The PDF file includes:

Materials and Methods
Supplementary Text
Figs. S1 to S19
Tables S1 to S4
References

List of contents

1 Materials and Methods	4
1.1 Preparation of Urethane Solutions and Fabrication of Urethane Fabry-Pérot Cavities	4
1.2 Angle-Dependent Transmittance Measurement using Fourier-Transform Infrared (FTIR) Spectrometer	5
1.3 Data Processing	5
2 Infrared Signatures of Reactants and Products	6
3 Measuring reaction rates from transmission measurements	9
3.1 Out-of-Cavity Reaction Rate Measurements	10
3.2 Coupled Cavity Dispersion Plots for Reactants and Product Modes	11
3.3 Cavity-Coupled Reaction Rate Measurements	11
4 Electronic Structure and Normal Mode Analysis	19
4.1 Phenyl Isocyanate: Fundamental and Combination Modes	19
4.2 Cyclohexanol, Tetrahydrofuran and Cyclohexyl	20
5 Modeling Cavity-Free Infrared Absorption of Phenyl Isocyanate	22
5.1 Vibrational Quantum Master Equation	22
5.2 Model calibration with the experimental absorption spectrum	24
6 Intracavity chemical reaction rate model	25
6.1 Single-Molecule Theory	27
6.2 Analytical Approximations	29
6.3 Redfield Quantum Master Equation in the Polariton Basis	34
6.3.1 Canonical Thermal versus non-Canonical Steady States	36
6.3.2 Spectroscopic Equivalence of Lindblad and Redfield Models	37

6.4	Many-body cavity chemistry	38
6.4.1	Truncated equations of motion including Fermi resonance	38
6.4.2	Cavity-dependent vibrational occupations with energy disorder	42
7	Comparison with Previous Models	46

1 Materials and Methods

1.1 Preparation of Urethane Solutions and Fabrication of Urethane Fabry-Pérot Cavities

Equimolar solutions of cyclohexanol (#105899, Sigma-Aldrich) and phenyl isocyanate (#185353, Sigma-Aldrich) were prepared by dissolving each in anhydrous tetrahydrofuran (Sigma-Aldrich) to concentration of 3 mol/L. Urethane solution was made by mixing those prepared cyclohexanol and phenyl isocyanate solutions at 1:1 volume ratio prior to injection into a liquid cell. A Fabry-Pérot cavity was fabricated by deposition of Cr/Au film (3/18 nm in thickness) on CaF_2 windows using an electron-beam evaporator (Temescal model FC-2000). The Cr film was deposited to improve adhesion of the Au film onto the CaF_2 window. In order to avoid potential chemical perturbation on the Au film by urethane solution, a SiO_2 layer (200 nm in thickness) was deposited on top of the Au film using a magnetron sputtering system (AJA International Inc). For out-of-cavity control, SiO_2 film was deposited on bare CaF_2 windows that are free of Au film. An FTIR cell consisted of two CaF_2 windows (that are Au/ SiO_2 coated for a cavity sample and SiO_2 coated for an out-of-cavity control) and a PTFE spacer (with path-lengths varied from 6 to 12 μm , Harrick Scientific Products). The cell was assembled using chemically-resistant Kalrez O-rings and sealed with lightly-applied vacuum-greased plugs. The volume of the urethane solution in the cell was estimated as ~ 2 or $\sim 4 \mu\text{L}$ when a 6 or 12 μm -thick spacer was used. Temperature and humidity was maintained at $22.0 \pm 0.3^\circ\text{C}$ and 18 % throughout the measurement.

Two types of windows were used, round 1" diameter or rectangular 41 \times 23 mm. In all cases, the windows were 2 mm thick. Beam spot size is important since it, along with cavity parallelism, determines the range of cavity tunings probed. In our case, the probe beam was apertured down to 2 mm, which spanned 1/4 of a visible fringe. Each visible fringe indicates a variation in the cavity length equal to the visible wavelength divided by the refractive index ($600 \text{ nm}/1.4 = 429 \text{ nm}$). One quarter of this is 100 nm, which would correspond to a range of infrared cavity resonances spanning 30 cm^{-1} at 2200 cm^{-1} (roughly the size of the data point

symbols in Fig. 2 of the main text).

1.2 Angle-Dependent Transmittance Measurement using Fourier-Transform Infrared (FTIR) Spectrometer

Angle-dependent transmittance spectra of the solution-filled cavity were obtained using a Fourier-transform infrared (FTIR) spectrometer (Thermo Scientific) equipped with a home-built sample rotator (BGM80, Newport), which allowed light to be incident upon the cavity at an angle ranging from -10° to 70° . A MCT detector was used in the FTIR spectrometer, with the unpolarized light centered at the cavity with a mechanical aperture. The system was controlled by LabVIEW program to collect the transmittance spectra of the cavity with 1° interval in the spectral range of $650\text{--}7000\text{ cm}^{-1}$. Time series scans were taken over either ≈ 10 or 24 hrs. A background spectrum was obtained using an empty sample holder under the same acquisition conditions that were used for the sample measurements (number of scans of 64, resolution of 4, scan speed of 1.8988, and aperture size of 4).

1.3 Data Processing

The transmittance spectra measured at varying incident angles were compiled using a custom-written Igor program (Igor Pro. v6.3.7.2.) to plot the dispersion curve of the transmission spectra as a function of wavenumber vs. angle. The angle at which the cavity mode is tuned to the reactant NCO mode are identified and those spectra extracted are fitted to the following expression for transmission through a Fabry-Pérot cavity

$$T_{\text{cav}}(\nu) = \frac{(1 - R)^2 e^{-\alpha L}}{1 + R^2 e^{-2\alpha L} - 2R e^{-\alpha L} \cos(4\pi n L + 2\phi)}, \quad (\text{S1})$$

where ν is frequency, R mirror reflectivity, L the cavity length, $n = \sqrt{(\varepsilon_1 + \sqrt{\varepsilon_1^2 + \varepsilon_2^2})/2}$ the intracavity refractive index, $\alpha = 4\pi\nu\sqrt{(-\varepsilon_1 + \sqrt{\varepsilon_1^2 + \varepsilon_2^2})/2}$ the absorption coefficient, and ϕ the phase shift upon reflection. The frequency dependence of n and α is modeled using the

Lorentzian response functions

$$\varepsilon_1 = n_{\text{bg}}^2 + \sum_i \frac{A_i(\nu_i^2 - \nu^2)}{(\nu_i^2 - \nu^2)^2 + (\Gamma_i \nu)^2} \quad (\text{S2})$$

and

$$\varepsilon_2 = \sum_i \frac{A_i \Gamma_i \nu}{(\nu_i^2 - \nu^2)^2 + (\Gamma_i \nu)^2}. \quad (\text{S3})$$

Equation (S1) is fit to the experimental data with the Lorentzian oscillator amplitudes, A_i as fitting parameters. This amplitude is converted to [PHI] via calibration measurements of concentration-dependent PHI absorption (calibration in Fig. S3). Example data and fits are shown in Fig. S4 (spectra and reaction rate data for all samples in Fig. S6 and summarized in Table S1). All data abide reasonably to linear fits whose slopes are the second order reaction rate constant.

For out-of-cavity controls, absorbance spectra were taken at a normal angle of incident light every 40 min for ~ 24 hrs. Absorbance peaks were fitted with a Lorentzian function (Origin Pro. 2017) to get integrated peak areas of the NCO band at 2270 cm^{-1} (A_{NCO}) that decrease as urethane formation proceeds. In a separate experiment, we measured absorbance of phenyl isocyanate solutions with 7 different concentrations ([PHI] ranged from 0 to 1.5 M) in order to obtain a calibration curve between [PHI] and A_{NCO} . Similar to the cavity-coupled samples, the second order reaction constant (k) was obtained from the slope of a linear plot between $1/[\text{PHI}]$ and time.

2 Infrared Signatures of Reactants and Products

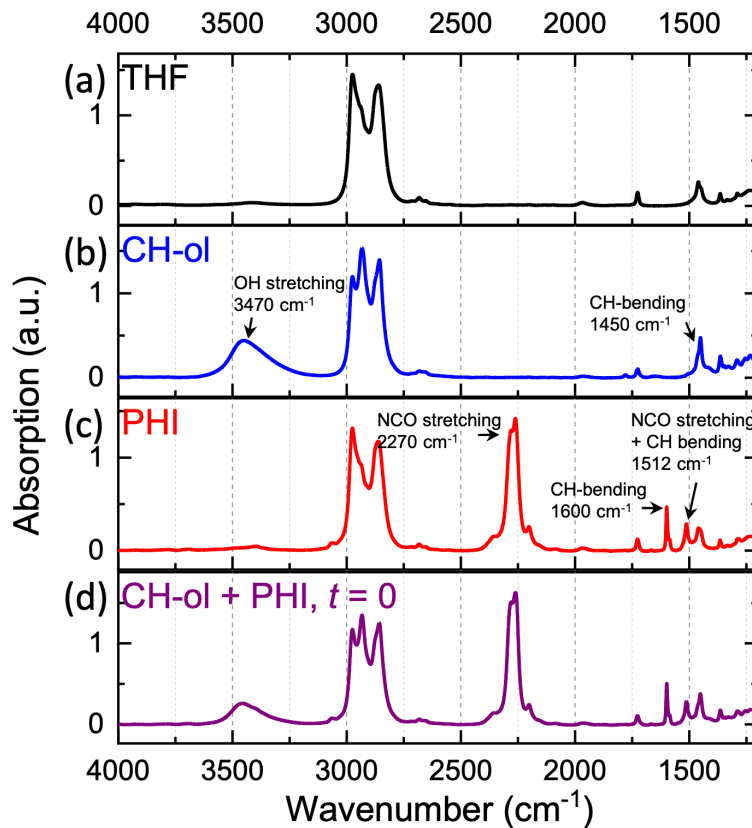


Figure S1: Infrared absorption spectra for all species. The THF solvent (a) is dominated by a series of CH modes in the $2700\text{-}3000\text{ cm}^{-1}$ region. The alcohol, Ch-ol dissolved in THF, in (b) exhibits a broad OH stretch absorption at $\sim 3470\text{ cm}^{-1}$ (this only yields weak coupling) and contributes a new peak to the family of CH modes. The reactant PHI dissolved in THF, (c), is characterized by a very strong feature at $\sim 2270\text{ cm}^{-1}$. Though this feature is predominantly due to an asymmetric NCO stretch mode, there are two combination modes present as well which contribute shoulders to the blue and red of the primary peak. An absorption spectrum of the full reaction solution is shown in (d).

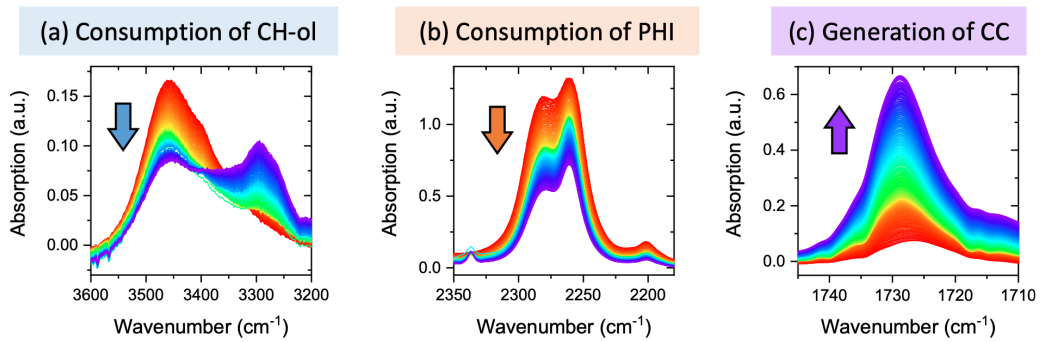


Figure S2: Time-dependent absorption spectra revealing consumption of reactants and production of products. (a) shows the high frequency region where Ch-ol OH modal absorption decays as an NH product mode arises. (b) shows decreasing intensity of the NCO-related modes as [PHI] concentration is reduced. Lastly, (c) shows the formation of the carbonyl product mode.

3 Measuring reaction rates from transmission measurements

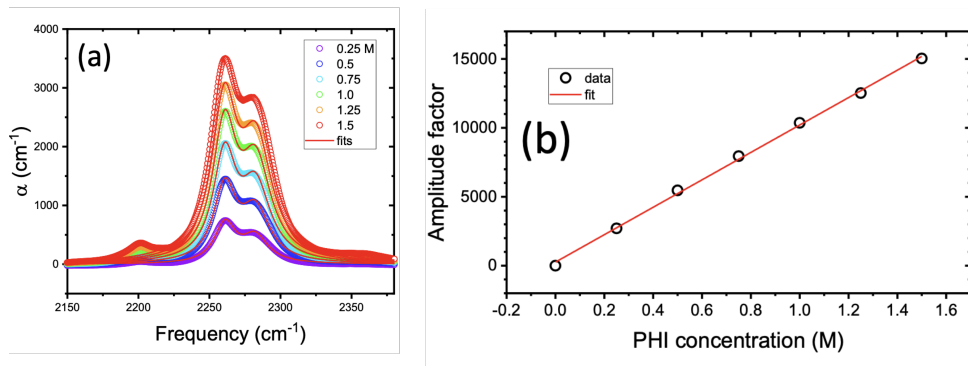


Figure S3: Calibration measurements used to extract [PHI] from out of cavity control experiments and cavity-coupled reactions. (a) shows absorption spectra for various concentrations of PHI in THF. For these data, raw absorbance (in OD), were converted to extinction coefficient then fit to a Lorentzian oscillator model consisting of two oscillators (fit results are solid curves). The fit parameters are resonant frequencies and amplitudes for the two oscillators. The oscillator frequencies from all of these fits were in reasonable agreement with one another and were averaged. Similar treatment was applied to the relative amplitudes between the two oscillators. In (b) the amplitude factor of the primary oscillator is plotted vs [PHI] (slope is proportional to the molar extinction coefficient). From these data, molecular concentration may be extracted from extracted absorption coefficients resulting from fits to either transmission or absorption spectra.

3.1 Out-of-Cavity Reaction Rate Measurements

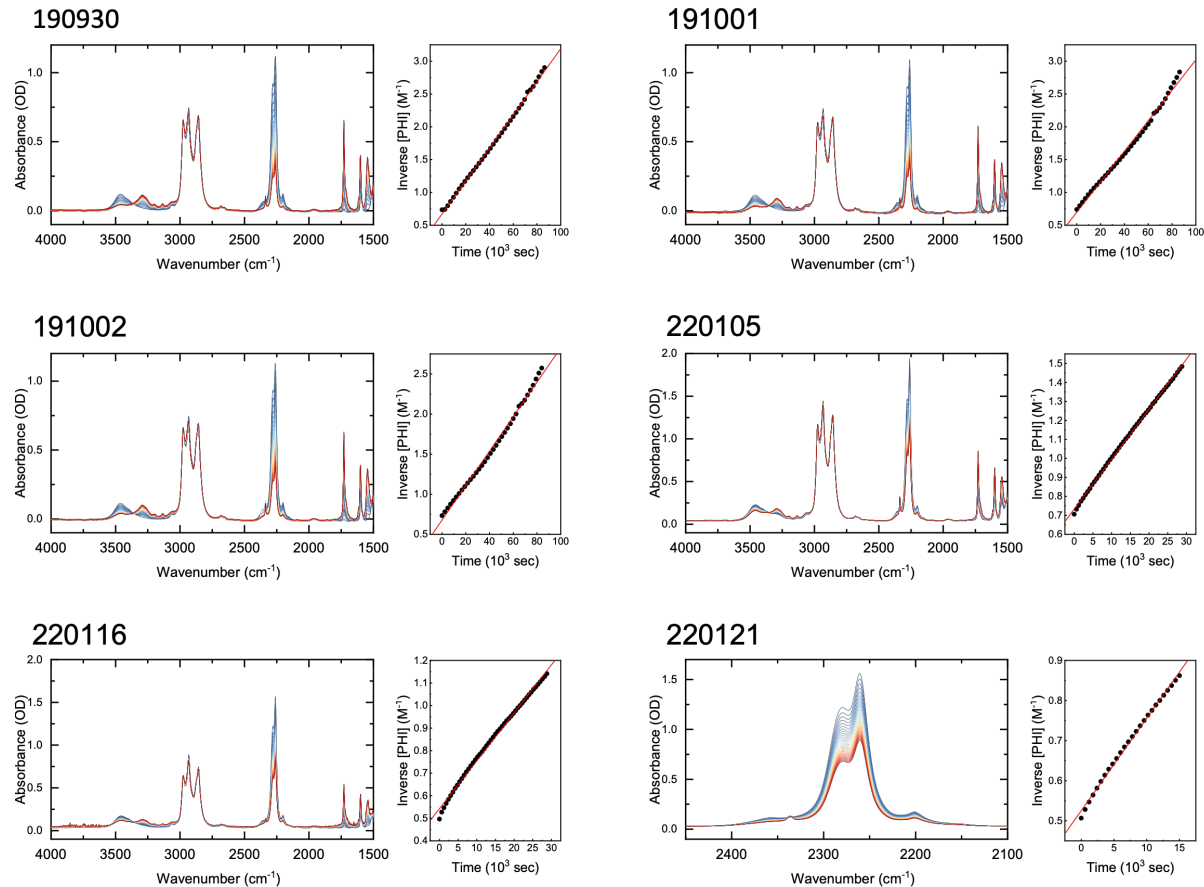


Figure S4: Raw spectra and reaction rate constant extraction for out-of-cavity controls. Sample name is given above each plot and is a date format ##year ##month ##day.

3.2 Coupled Cavity Dispersion Plots for Reactants and Product Modes

To examine the cavity-coupled environment, Fabry-Pérot cavities were prepared by assembling mirrors (CaF_2 coated with Au then SiO_2) separated by mylar spacers (thicknesses $\sim 6 - 9 \mu\text{m}$, schematic in Fig. S5b (see table of cavity thicknesses, resonance frequencies, and resulting rate constants in Table S1). The control spectra of Fig. 1c from the main text is reproduced in Fig. S5a, but plotted as transmission, to enable a direct correlation between targeted vibrational bands and cavity mode positions. We show four example sets of cavity transmission spectra, taken at normal incidence, for cavities tuned to (c) ν_{CH} , (d) ν_{NCO} , (e) ν_{CO} , and (f) detuned from all bands (spectra shown in blue to red taken every 40 min for 24 hrs). For each, a shaded area denotes the spectral region where a cavity mode is tuned to a relevant molecular vibration. Dispersions of these same cavities are shown for the initial (c1 - f1) and final times (c2 - f2). Several important features are apparent. First, one must consider the fidelity with which a given vibrational band may be targeted. The cavity quality factor is $Q \sim 100$ (linewidth at 2640 cm^{-1} is 24.9 cm^{-1}) and the free spectral range is $\sim 450 \text{ cm}^{-1}$ indicating that the reactant, product, and solvent bands can each be targeted with minimal unintentional coupling to other bands (time-dependent spectra for all cavity tunings are provided in Fig. S4). Second, strong coupling is achieved for ν_{CH} , ν_{NCO} and ν_{CO} bands with Rabi splitting to molecular linewidth ratios of 188/157, 112/41, and 38/19, respectively (modal linewidths, Rabi splittings, and their ratios are found in Table S2).

3.3 Cavity-Coupled Reaction Rate Measurements

Evolution of the coupling strength occurs as reactants are consumed and products created. This reduction or formation of a Rabi splitting is evident in both the time-dependent spectra and the associated dispersions (compare initial and final dispersions Fig. S5d1, d2 which show splitting reduction and e1, e2 which show the development of splitting). This time-dependent splitting is examined below and is simply a demonstration of the Rabi splitting's dependence on the square root of coupled species concentration. On the other hand, for the cavity tuned to the CH mode

(present in the CH-ol and the THF solvent), the Rabi splitting remained constant over the course of the reaction (Fig. S5c1, c2) since solvent concentration dominates and remains constant.

The dispersions also demonstrate that while a particular cavity may be detuned from the NCO reactant band at normal incidence, the cavity resonance may tune to that band at higher incident angle enabling extraction of the Rabi splitting and a direct measure of the species concentration through evaluation of these higher angle spectra (see Fig. S5f1, f2). Examination of these spectra will provide the basis for tracking the reaction progress. Lastly, we point out shifting of the cavity mode fringes with time. We found this shift generally moved toward lower frequency with time although was less well-behaved at early times. This shift has been attributed to evolving background refractive index of the solution as reactants convert to product species and was recognized by the Ebbesen group as an effective means for monitoring chemical reaction progress. Although we initially intended to adopt this same approach, instability in the early time cavity resonances resulted in unreliable data. The early-time instability in the shift of the cavity mode fringes may originate from “settling” of the cavity (relaxation of spacers, O-rings, or fasteners or solvent evaporation into any headspace that might exist in the cavity fixture fill ports). These instabilities motivated us to analyze reaction progress using direct fitting of the strongly coupled spectra.

The absorption coefficient of the material inside the cavity is directly expressed in its transmission function. An example of this treatment is shown in Fig. S5. For each time, a full dispersion is collected. Spectra collected at an angle where the cavity mode is tuned to the reactant ν_{NCO} mode are extracted and fitted to the following expression for transmission through a Fabry-Pérot cavity [44]

$$T_{\text{cav}}(\nu) = \frac{(1 - R)^2 e^{-\alpha L}}{1 + R^2 e^{-2\alpha L} - 2R e^{-\alpha L} \cos(4\pi n L \nu + 2\varphi)}, \quad (\text{S4})$$

where ν is frequency, R the mirror reflectivity, α the absorption coefficient, L the cavity length, n the refractive index, and φ the optical phase shift upon reflection. Both α and n are frequency-dependent and are described by a Lorentzian oscillator model. The amplitude of the Lorentzian oscillator associated with the NCO mode absorption can be quantitatively

correlated with reactant concentration with the help of the calibration measurements in Fig. S3. We extract the Lorentzian oscillator amplitude via fit, convert it to [PHI] via the calibration, invert, and plot as a function of time. Data obtained from this procedure is show Fig. S8. All data abide reasonably to linear fits whose slopes are the second order reaction rate constant.

Although the data as a whole are not abundant enough for a comprehensive examination of correlations between coupling strength, linewidths, and the ability to modify reaction kinetics, we point out that, in our study, the splitting to molecular linewidth ratio, $F_\Gamma \equiv \Omega/\Gamma$ is $\sim 2.95, 1.22, 2.34$ for coupling to the ν_{NCO} , ν_{CH} , and ν_{CO} , respectively. There is evidence that the degree to which a given reaction is modified would depend on the Rabi splitting of that band [8, 9). We can then associate the susceptibility of a given mode to cavity-induced rate modification to the reaction rate constant modification divided by splitting to linewidth ratio. Our data thus give the sensitivity parameters, $B_\Gamma \equiv [(k_{\text{vib.band}} - k_{\text{cntrl}})/k_{\text{cntrl}}]/F$ equals to -0.27 , -0.41 , and -0.21 for the ν_{NCO} , ν_{CH} , and ν_{CO} , respectively. If, instead, the factor F were calculated as the splitting normalized to the mode frequency, a common approach to distinguishing between coupling regimes, $F_\nu = \Omega/\nu$ would be $\approx 0.051, 0.065$, and 0.022 , yielding sensitivity parameters, B equals to -15.7 , -7.7 , and -22.7 , again referring to the ν_{NCO} , ν_{CH} , and ν_{CO} , respectively. These treatments and values are all summarized in Table S2.

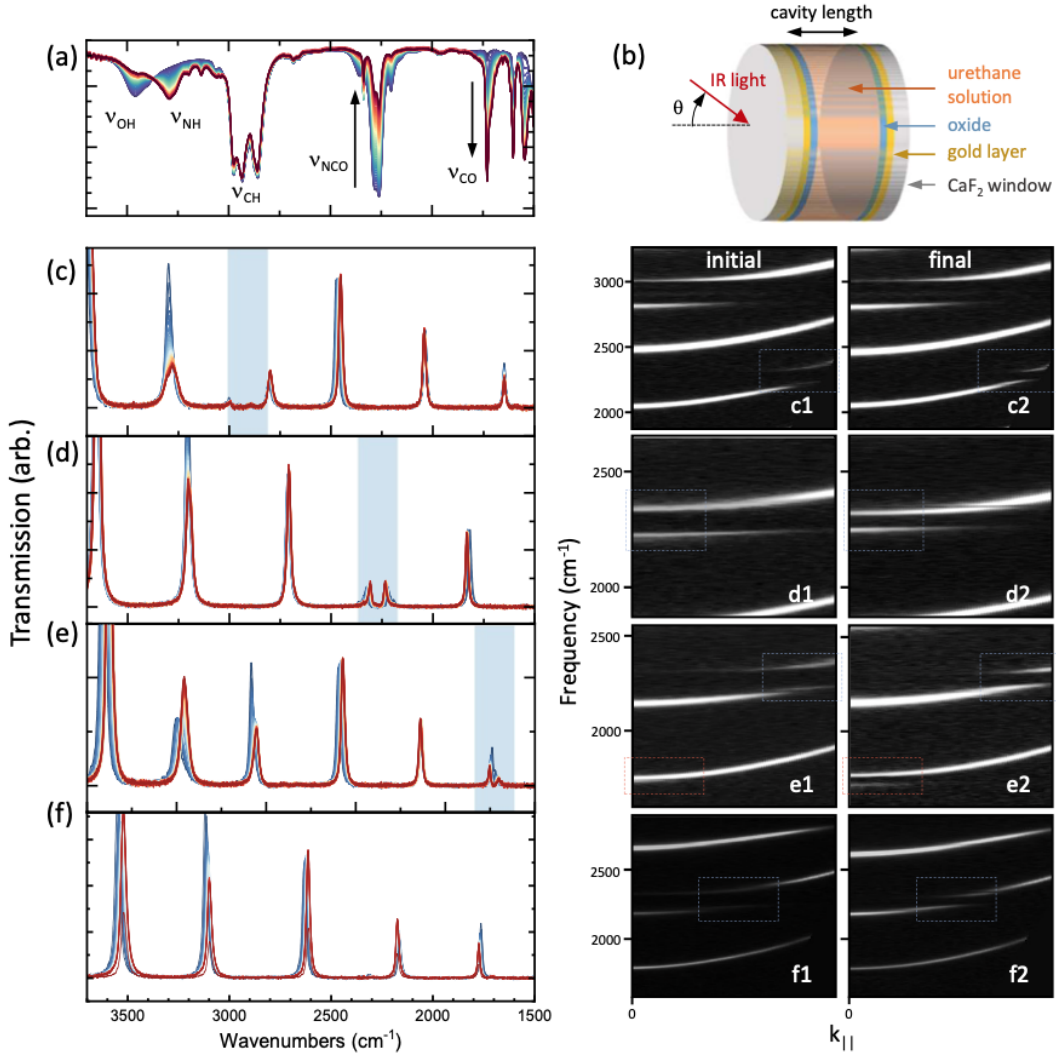


Figure S5: Description of reaction carried out inside cavities. (a) Time-dependent out-of-cavity transmission spectra to be used as a reference for indicating resonant molecular vibration positions and (b) schematic of the Fabry-Perot cavity in which the urethane formation is monitored. Note that the windows have a layer of Au resulting in cavity resonances with $Q \sim 90$ and free spectral range $\approx 420 \text{ cm}^{-1}$. Time-dependent transmission spectra for several typical cavities are shown in (c)-(f). These are examples demonstrating cavities whose resonances are aligned to (c) solvent CH, (d) reactant NCO, (e) product CO, and (f) detuned from all relevant bands. Dispersions (c1,2) – (f1,2) correspond to the similarly labeled cavities at (1) initial and (2) final reaction times. Splitting due to reactant modes are seen to reduce and splitting associated with coupling to products grow over time.

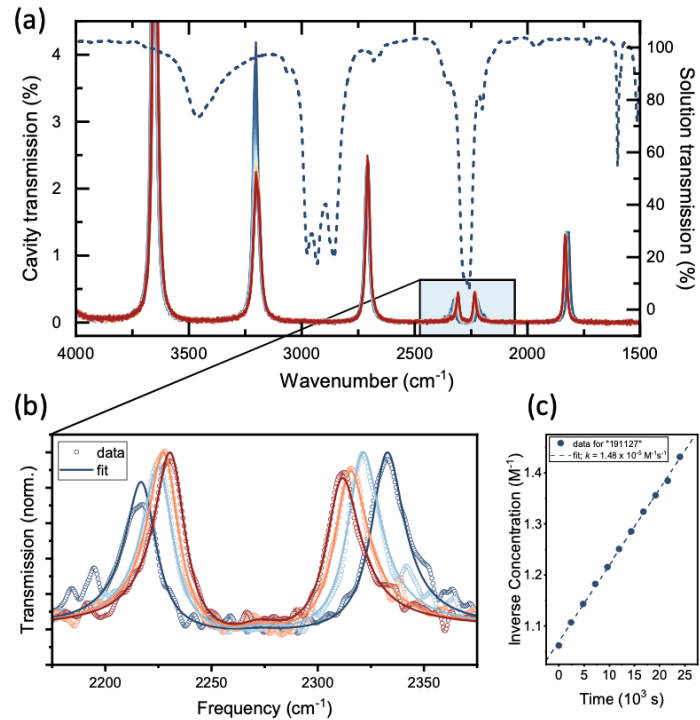


Figure S6: Examination of cavity coupled reaction rate extraction. First, (a) show time-dependent transmission spectra through a cavity tuned to the PHI reactant NCO mode. The transmission of the uncoupled solution is also shown (dashed) for reference to pertinent peak positions. (b) displays a selection of cavity coupled spectra in the spectral region described by strong coupling between the cavity and NCO mode. Each spectrum can be fit to Eq. (S1) to yield extinction coefficient, as a function of time (data are dots, fits are solid line curves). These values for are converted to [PHI] then inverted and plotted as shown in (c). The slope of the resulting linear fit is the second order reaction rate constant.

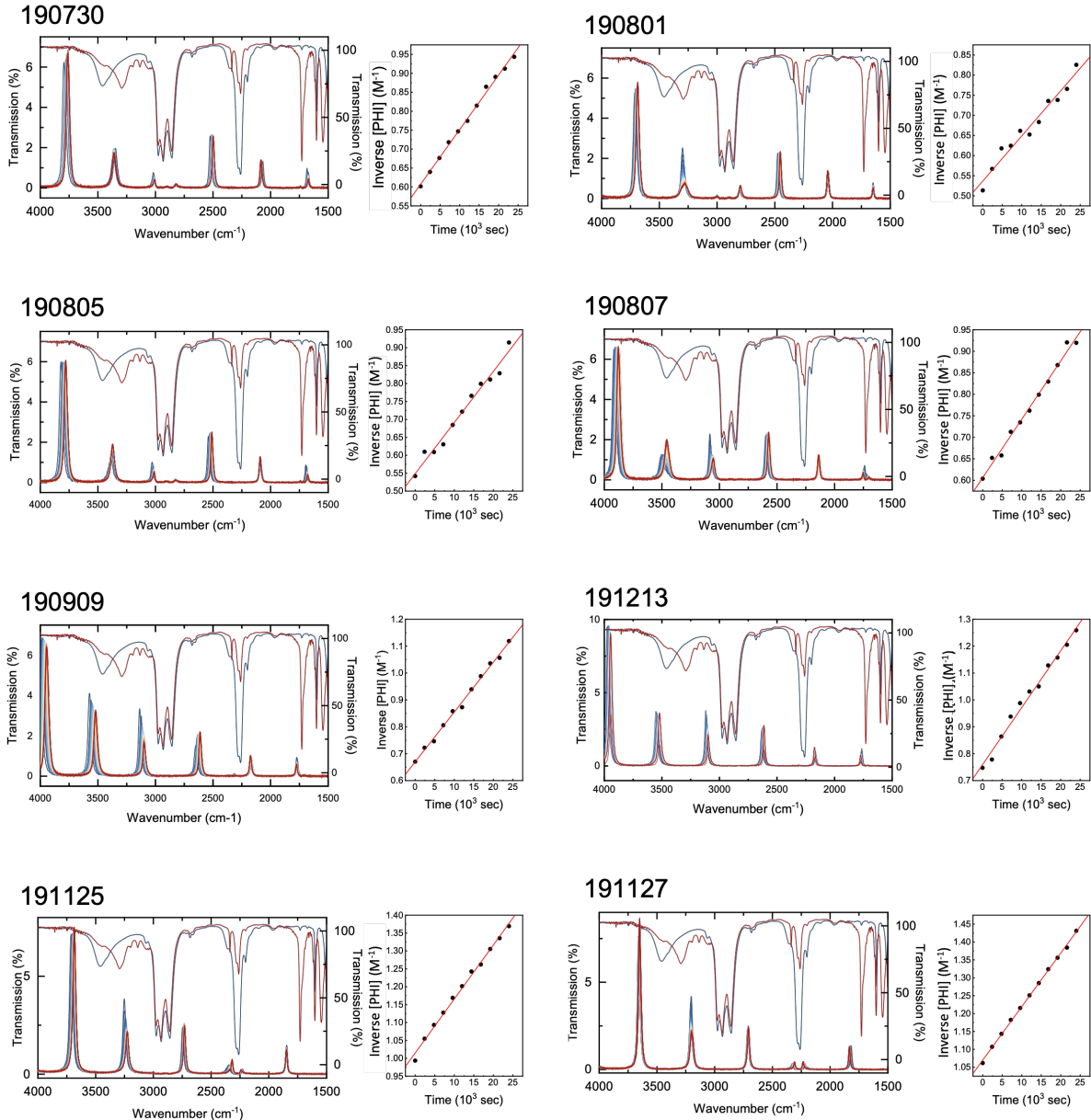


Figure S7: Complete data sets from which we extract cavity coupled and out of cavity control reaction rate constants. Here we include the raw spectra acquired at normal incidence, and the inverted $[\text{PHI}]$ values with linear fits. Sample name is given above each plot and is a date format `##year ##month ##day`.

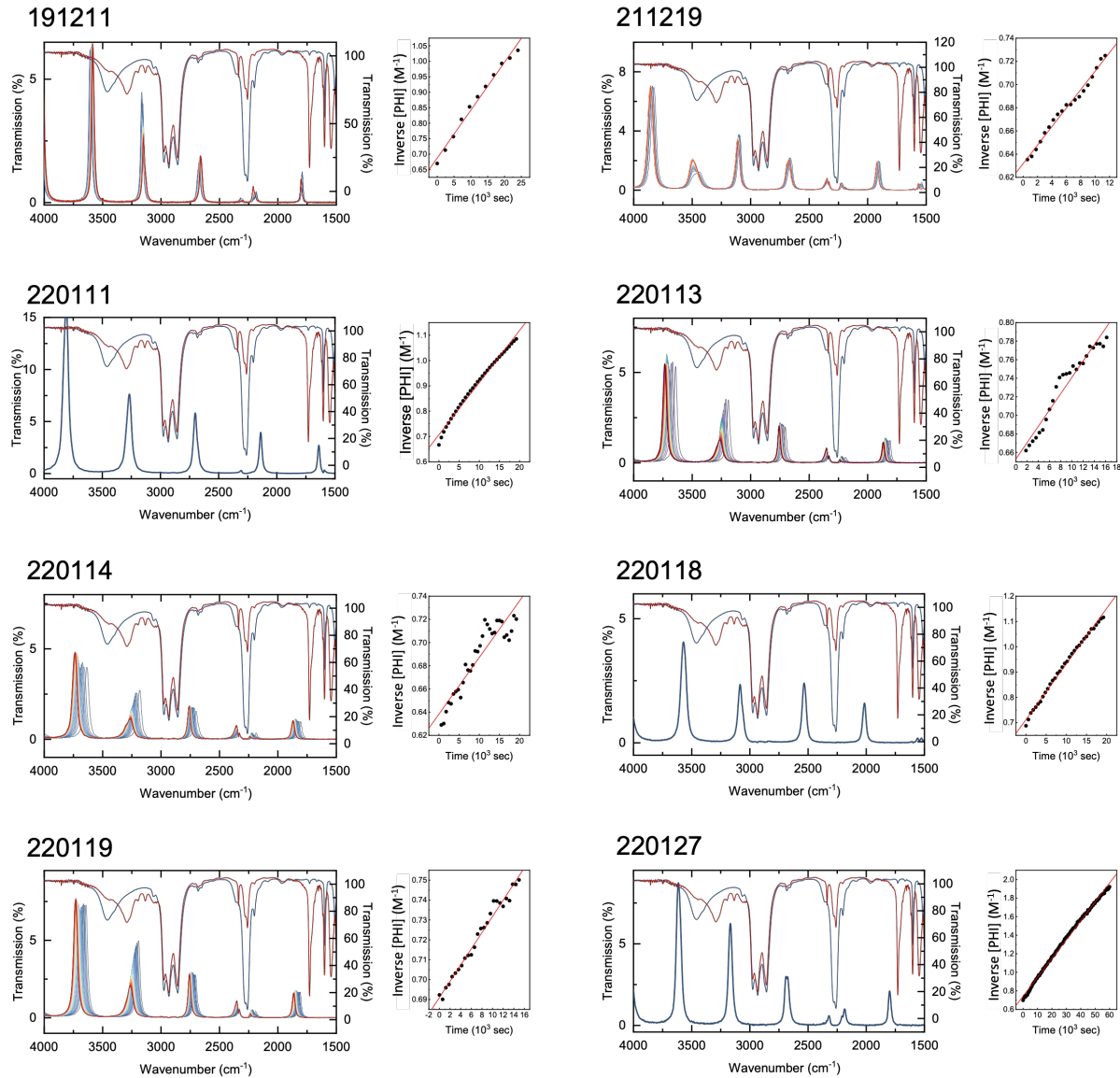


Figure S8: Complete data sets from which we extract cavity coupled reaction rate constants. Here we include the raw spectra acquired at normal incidence, and the inverted $[\text{PHI}]$ values with linear fits. Sample name is given above each plot and is a date format ##year ##month ##day.

Sample date (yr mo day)	Cav. Thickness (mm)	Res. Position (cm ⁻¹)	Reaction rate constant (M ⁻¹ s ⁻¹ × 10 ⁻⁵)
Out of cavity controls			
220121	7.34		2.30
220116	7.23		2.13
220105	12.3		2.63
190930	7.984	Out of cavity controls	2.52
191001	7.799		2.32
191002	8.042		2.15
		Average of out of cavity controls	2.34 (±0.20)
Tuned at or near OCN mode			
190909	7.739	2216	1.86
191125	7.75	2304	1.51
191127	7.78	2252	1.48
191211	8.04	2236	1.55
191213	8.223	2214	1.56
220127	8.03	2024	2.03
211219	9.015	2290	0.77
220113	7.87	2301	0.726
220114	7.99	2299	0.486
220119	7.85	2290	0.408
Tuned to solvent OH modes			
190730	8.228	2940	1.44
190801	8.505	2870.7	1.21
190805	8.19	2959.3	1.43
Tuned to product CO mode			
190807	7.887	1735	1.36
Detuned from all relevant modes			
220111	6.6	1617, 2156, 2696, 3225	2.06
220118	6.83	1502, 2002, 2502, 3003	2.2

Table S1: Summary of data, sample parameters and reaction rate constants.

ν (cm ⁻¹)	Γ (cm ⁻¹)	Ω (cm ⁻¹)	$\Delta k = \frac{(k_{\text{vib,band}} - k_0)}{k_0}$	B_ν	B_Γ	B_Ω
NCO 2260	38	112	-0.8	-15.7	-0.27	-0.007
OH 2900	154	188	-0.5	-7.7	-0.41	-0.003
CO 1730	17	38	-0.5	-22.7	-0.21	-0.013

Table S2: Summary of vibrational frequencies (ν), linewidths (Γ), Rabi splittings (Ω), and proposed sensitivity parameters $B_\nu \equiv \Delta k \cdot \nu / \Omega$, $B_\Gamma \equiv \Delta k \cdot \Gamma / \Omega$, $B_\Omega \equiv \Delta k / \Omega$.

4 Electronic Structure and Normal Mode Analysis

First-principles electronic structure calculations were carried out to study the vibrational normal modes of Phenyl Isocyanate (PHI), tetrahydrofuran (THF), cyclohexanol (CH-ol) in gas phase using the software MOLPRO [45]. Initial ground state geometry optimizations were done at the CCSD level of theory using Dunning’s aug-cc-pVDZ basis set. Normal mode frequencies were found using the “harmonic vibrational frequencies” option in the MOLPRO package. This generates IR absorption frequencies and intensities. For cyclohexyl, normal mode frequencies were obtained using DFT with a CAM-B3LYP/6-311++G level of theory [46]. Although all the *ab-initio* calculations are performed in gas phase, preliminary MOLPRO calculations remark that a normal mode calculation with implicit solvent only generates red shifts [46], which do not change substantial the results and analysis described in the main text.

4.1 Phenyl Isocyanate: Fundamental and Combination Modes

The gas-phase fundamental vibration frequencies of phenyl isocyanate (Cs symmetry) are given in Table S3. This molecule has a very strong IR active fundamental mode at 2259 cm^{-1} denoted ν_6 , corresponding to an NCO stretch. The atomic displacements in the ν_6 mode are illustrated in Fig. S9. There are also four combination bands with IR active peaks of varying strengths in the region near the ν_6 fundamental, which we denote by ν_{C1} , ν_{C2} , ν_{C3} and ν_{C4} , in order of increasing frequency. The atomic displacements for the components of these four combination modes are illustrated in Fig. S10. The weak combination mode $\nu_{C1} = \nu_9 + \nu_{22}$ is about 200 cm^{-1} (gas phase) from the fundamental mode ν_6 . In this combined mode the N-C bond length is stretched by about 0.06 \AA . The second combination mode $\nu_{C2} = \nu_{14} + \nu_{18}$ is at 2197 cm^{-1} (gas phase) and has a strong IR response. Although it is red detuned from the ν_6 fundamental by only about 60 cm^{-1} , the analysis of atomic motions shows that the C-N and N-C bond distances do vary significantly ($\Delta d_{\text{CN}} < 0.003\text{ \AA}$, $\Delta d_{\text{NC}} < 0.008\text{ \AA}$) in comparison the displacements in the fundamental mode ν_6 ($\Delta d_{\text{CN}} = 0.13\text{ \AA}$, $\Delta d_{\text{NC}} = 0.056\text{ \AA}$). The third combination band $\nu_{C3} = \nu_{14} + \nu_{16}$ gives a very strong IR peak at frequency 2278 cm^{-1} with A' symmetry, which

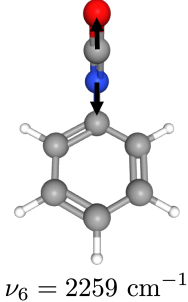


Figure S9: **NCO stretching mode of phenyl isocyanate:** Atomic displacements (black arrows) for the fundamental mode ν_6 of PHI, which involves linear stretching of the nitrogen (blue), carbon (grey) and oxygen (red) atoms.

is blue detuned from the main ν_6 fundamental by only 19 cm^{-1} . Figure S10c shows that both the ν_{14} and ν_{16} modes involve CH stretching in the phenyl ring, while the NCO group remains mostly at equilibrium ($\Delta d_{\text{CN}} = \Delta d_{\text{NC}} = 0.01 \text{ \AA}$). Finally, there is a weak combination band $\nu_{\text{C}4} = \nu_7 + \nu_{20}$ at 2365 cm^{-1} , blue detuned from ν_6 by about 100 cm^{-1} (Fig. S10d, gas phase). In this case, one of the fundamental modes it is not IR active (ν_{20}). This mode involves low-amplitude motion of $\Delta d_{\text{CN}} = 0.004 \text{ \AA}$ and $\Delta d_{\text{NC}} = 0.02 \text{ \AA}$. Due to their A' symmetry, all the combination modes in Fig. S10 are electric dipole allowed. As shown below, the $\nu_{\text{C}3}$ combination mode has a strong IR response with oscillator strength comparable to the main ν_6 fundamental.

4.2 Cyclohexanol, Tetrahydrofuran and Cyclohexyl

Cyclohexanol and tetrahydrofuran *ab initio* calculations in gas phase show that both molecules do not have fundamental vibrational modes in the region of interest ($2000\text{-}2500 \text{ cm}^{-1}$). For these species the fundamental modes are found below $\sim 1500 \text{ cm}^{-1}$ and above $\sim 3000 \text{ cm}^{-1}$, in agreement with previous work [48]. Although there are combination modes in the spectral region of interest, they correspond to atomic motions that do not involve the molecular bonds that are believed to participate in the urethane formation reaction [3].

Cyclohexyl does not have fundamental normal modes around the main ν_6 resonance of

Mode Index	Mode Symmetry	Exp. Mode Frequency (cm ⁻¹)	This work (cm ⁻¹)
ν_{25}	A'	100 (m)	82
ν_{35}	A''	246 (m)	243
ν_{24}	A'	384 (m)	389
ν_{34}	A''	410 (vw)	412
ν_{23}	A'	460 (m)	460
ν_{33}	A''	491 (m)	502
ν_{22}	A''	566 (m)	586
ν_{32}	A''	631 (m)	649
ν_{31}	A''	687 (vs)	665
ν_{30}	A''	751 (vs)	759
ν_{29}	A''	829 (w)	853
ν_{28}	A''	904 (m)	911
ν_{27}	A''	964 (vw)	970
ν_{26}	A''	983 (vw)	973
ν_{19}	A'	1005 (w)	1015
ν_{18}	A'	1025 (s)	1051
ν_{17}	A'	1071 (m)	1099
ν_{16}	A'	1108 (s)	1159
ν_{14}	A'	1170 (w)	1192
ν_{13}	A'	1281 (vw)	1297
ν_{12}	A'	1335 (vw)	1339
ν_{11}	A'	1445 (w)	1481
ν_{10}	A'	1451 (m)	1491
ν_9	A'	1510 (vs)	1575
ν_8	A'	1584 (s)	1661
ν_7	A'	1599 (vs)	1684
ν_6	A'	2259 (vvs)	2358
ν_5	A'	3029 (m)	3206

Table S3: **Normal mode frequencies of Phenyl Isocyanate (PHI):** Fundamental mode labels (ν_j), group symmetry representations, experimental mode frequencies and intensities from Ref. [47] (vw=very weak, w=weak, m=medium, s=strong, vs=very strong, vvs=very very strong), and *ab-initio* mode frequencies in gas phase (this work). The NCO stretching mode ν_6 and the benzene ring modes ν_{14} and ν_{16} are known to participate in the urethane formation reaction [3].

phenyl isocyanate (DFT frequency = 2430 cm⁻¹). The two fundamental modes involving N, C, O atoms with high IR response occur at 1235 cm⁻¹ and 1281 cm⁻¹ (gas phase). These two

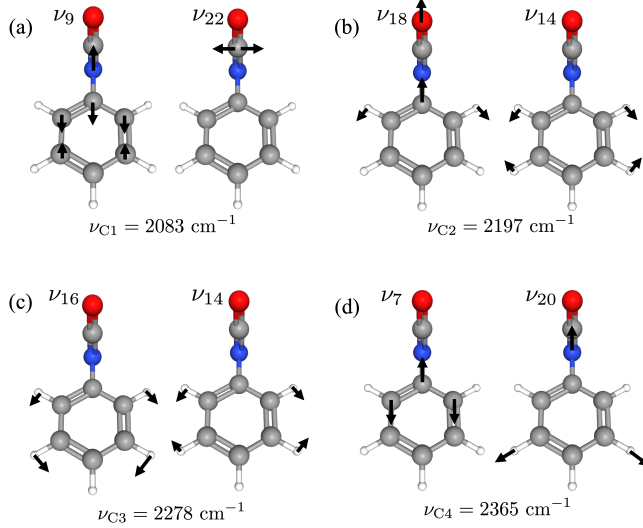


Figure S10: **Combination modes of phenyl isocyanate:** Atomic displacements (black arrows) for the fundamental modes that form the combination modes $\nu_{C1} = \nu_9 + \nu_{22}$ (2093 cm^{-1}), $\nu_{C2} = \nu_{18} + \nu_{14}$ (2197 cm^{-1}), $\nu_{C3} = \nu_{16} + \nu_{14}$ (2278 cm^{-1}) and $\nu_{C4} = \nu_7 + \nu_{20}$ (2365 cm^{-1}) of PHI molecules in gas phase.

modes form a combination band ν_{CH} at 2518 cm^{-1} .

5 Modeling Cavity-Free Infrared Absorption of Phenyl Isocyanate

5.1 Vibrational Quantum Master Equation

Based on the *ab-initio* normal mode analysis of PHI in gas phase, we assign the strong doublet feature around 2275 cm^{-1} in the free-space absorption spectrum to the fundamental mode ν_6 and combination band $\nu_{16} + \nu_{14}$ (ν_{C3}). The latter borrows electric dipole strength through a Fermi coupling mechanism with ν_6 [48]. We therefore model the cavity-free absorption spectrum of PHI (liquid phase) in the range $1900 - 2600\text{ cm}^{-1}$ using a total molecular Hamiltonian of the form $\hat{H}_S(t) = \hat{H}_0 + \hat{V}(t)$, where the first term is the effective vibrational Hamiltonian

$$\begin{aligned} \hat{H}_0 = & \omega_6 \hat{b}_6^\dagger \hat{b}_6 + \omega_{14} \hat{b}_{14}^\dagger \hat{b}_{14} + \omega_{16} \hat{b}_{16}^\dagger \hat{b}_{16} + \lambda (\hat{b}_{14}^\dagger \hat{b}_{16} + \hat{b}_{14} \hat{b}_{16}^\dagger) \\ & + \zeta_{14} (\hat{b}_{14}^\dagger \hat{b}_{14}^\dagger \hat{b}_6 + \hat{b}_{14} \hat{b}_{14} \hat{b}_6^\dagger) + \zeta_{16} (\hat{b}_{16}^\dagger \hat{b}_{16}^\dagger \hat{b}_6 + \hat{b}_{16} \hat{b}_{16} \hat{b}_6^\dagger), \end{aligned} \quad (\text{S5})$$

which describes the bare oscillations and interactions between the high-frequency NCO mode ν_6 and the low-frequency ring modes ν_{14} and ν_{16} of PHI. ω_j ($j = \{6, 14, 16\}$) are the bare frequencies, and λ is the coupling constant for the bilinear coupling between ν_{14} and ν_{16} . The coupling constants ζ_{14} and ζ_{16} give rise to the Fermi resonance $\nu_6 \leftrightarrow (\nu_{14} + \nu_{16})$, which is important to understand the vibrational spectrum of PHI in the region of interest. The time-dependent perturbation is $\hat{V}(t) = -\hat{d} \cdot \mathcal{E}(t)$, with $\mathcal{E}(t)$ being a driving cw laser field of real amplitude E_d , and \hat{d} is a vibrational dipole moment operator given by

$$\hat{d} = d_e + f_6(\hat{b}_6^\dagger + \hat{b}_6) + f_{C3}(\hat{b}_{14}^\dagger \hat{b}_{16}^\dagger + \hat{b}_{14} \hat{b}_{16}), \quad (S6)$$

where d_e is the equilibrium dipole moment of PHI, f_6 is the transition dipole of fundamental mode ν_6 , and f_{C3} the transition dipole of the combination mode ν_{C3} .

To build a reliable minimal model for the vibrational dynamics of PHI that is responsible for the infrared response in the region $2100 - 2600 \text{ cm}^{-1}$, the total system Hamiltonian $\hat{H}_S(t)$ must be supplemented by a microscopic description of vibrational relaxation for high and low frequency modes. For this we adopt a Lindblad quantum master equation of the form ($\hbar \equiv 1$)

$$\dot{\hat{\rho}} = -i[\hat{H}_S, \hat{\rho}] + \mathcal{R}_\gamma[\hat{\rho}] \quad (S7)$$

where $\rho(t)$ is the reduced vibrational density matrix, $\hat{H}_S(t)$ is the total system Hamiltonian described above, and the relaxation superoperator is given by

$$\mathcal{R}_\gamma[\hat{\rho}] = -\sum_j \left[\frac{\gamma_j(n_j^{\text{th}} + 1)}{2} \left(\hat{b}_j^\dagger \hat{b}_j \hat{\rho} - 2\hat{b}_j \hat{\rho} \hat{b}_j^\dagger + \hat{\rho} \hat{b}_j^\dagger \hat{b}_j \right) + \frac{\gamma_j n_j^{\text{th}}}{2} \left(\hat{b}_j \hat{b}_j^\dagger \hat{\rho} - 2\hat{b}_j^\dagger \hat{\rho} \hat{b}_j + \hat{\rho} \hat{b}_j \hat{b}_j^\dagger \right) \right], \quad (S8)$$

with j running over the three mode indices ν_j in the problem. The first term in the square brackets describes relaxation (cooling) of the vibrational energy into a thermal bosonic reservoir (e.g., other low-frequency vibrational modes, solvent modes) at the zero-temperature rate γ_j . The second term describes thermal excitation of vibrational modes through energy absorption from the thermal reservoir. $n_j^{\text{th}} = (\exp[\omega_j/k_B T] - 1)^{-1}$ is the thermal boson occupation number at the mode frequency ω_j . This form of the dissipator ensures that the vibrational modes

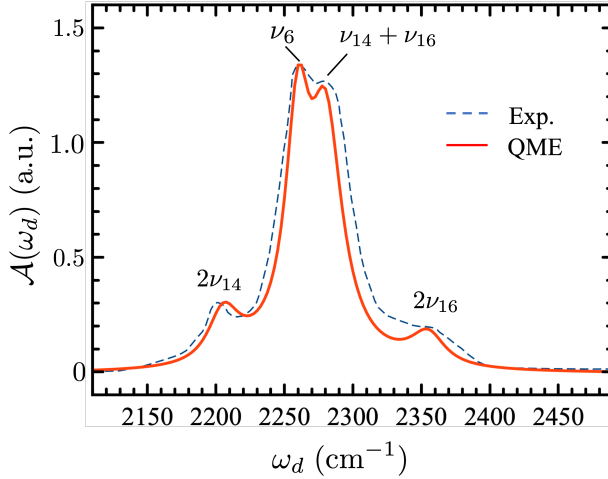


Figure S11: Infrared absorption spectrum of phenyl isocyanate in hexane in the region near the ν_6 NCO stretching band, in arbitrary absorbance units. The experimental data (dashed line) is normalized to coincide with the quantum master equation lineshape (solid line) at the peak of the ν_6 band. Peak assignments are discussed in the text.

equilibrate with the thermal bath in the absence of light-matter interaction, i.e., $\langle \hat{b}_j^\dagger \hat{b}_j \rangle = n_j^{\text{th}}$ for $t \gg \max\{\gamma_j^{-1}\}$.

5.2 Model calibration with the experimental absorption spectrum

The Lindblad quantum master equation in Eq. (S7) has free parameters that we calibrate by comparing the model infrared absorption spectrum in the range $2100 - 2600 \text{ cm}^{-1}$ with experimental data at room temperature. We compute the theoretical absorption at the driving frequency ω_d from the total vibrational occupation number in the steady state as $\mathcal{A}(\omega_d) \equiv \langle \hat{b}_6^\dagger \hat{b}_6 \rangle_{\text{ss}} + \langle \hat{b}_{14}^\dagger \hat{b}_{14} \rangle_{\text{ss}} + \langle \hat{b}_{16}^\dagger \hat{b}_{16} \rangle_{\text{ss}}$. In the linear response regime, this quantity is proportional to the number of absorbed photons from the monochromatic incident field at ω_d [49]. The steady state density matrix $\hat{\rho}(t \rightarrow \infty)$ is obtained by propagating a thermalized initial state $\hat{\rho}(0)$ over timescales $t \gg 1/\gamma_j$, under continuous driving with a monochromatic field at ω_d whose amplitude satisfies the inequality $f_6 |E_d| / \gamma_6 \ll 1$. The latter enforces linear response.

The fundamental mode ν_6 at $\omega_6 = 2260 \text{ cm}^{-1}$ and the combination band near 2280 cm^{-1}

are the strongest bands in the frequency region of interest. From the measured oscillator strengths, their dipole moment ratio is set to $f_6/f_{C3} = 1.14$. The model parameters that must be calibrated in the master equation [Eq. (S7)] are the bilinear coupling strength λ , the Fermi couplings (ζ_{14}, ζ_{16}), and the vibrational relaxation rates (γ_{14}, γ_{16}). Bare mode frequencies are obtained from additional experiments and *ab-initio* calculations. We set up a grid over these free parameters and compute an ensemble of theoretical absorption spectra $\mathcal{A}(\omega_d)$ for a given driving frequency ω_d . Minimizing the difference between the experimental and theoretical spectra over a range of driving frequencies, gives the model infrared absorption lineshape in Fig. S11, which corresponds to the set of optical parameters in Table S4. Figure S11 shows that the effective quantum master equation can accurately reproduce the weak overtone of ν_{14} at 2200 cm^{-1} , the strong ν_6 fundamental at 2260 cm^{-1} , the strong combination band $\nu_{14} + \nu_{16}$ at 2280 cm^{-1} , and the weak overtone of ν_{16} at 2350 cm^{-1} .

Parameter	Symbol	Value [cm ⁻¹]
ν_6 fundamental frequency	ω_6	2260.0
ν_{14} fundamental frequency	ω_{14}	1175.0
ν_{16} fundamental frequency	ω_{16}	1105.0
ν_{14} - ν_{16} bilinear coupling	λ	8.2
ν_6 - ν_{16} Fermi coupling	ζ_{14}	13.0
ν_6 - ν_{14} Fermi coupling	ζ_{16}	9.8
ν_6 vibrational relaxation rate	γ_6	20.2
ν_{14} vibrational relaxation rate	γ_{14}	15.3
ν_{16} vibrational relaxation rate	γ_{16}	14.0

Table S4: Calibrated model parameters for the vibrational quantum master equation [Eq. (S7)] that describes the reduced vibrational dynamics of phenyl isocyanate (PHI) in hexane outside a cavity.

6 Intracavity chemical reaction rate model

Following previous works [50, 51], we assume the intracavity reaction rate constant reactants to products can be factored as

$$k = \kappa(T)k_{\text{TST}}(T), \quad (\text{S9})$$

where $k_{\text{TST}}(T)$ is the Arrhenius rate constant outside the cavity at temperature T and $\kappa(T) = 1 + \xi(T)$ is a transmission factor that describes either the stationary suppression ($\xi < 0$) or enhancement ($\xi > 0$) of the rate constant due to light-matter interaction inside a cavity at T . We assume that, to lowest order, $\xi(T)$ is *proportional* to the deviation from the thermal (Boltzmann) vibrational population distribution in an ensemble of N reactive molecules at temperature T , for timescales that are much longer than the intrinsic coherent and dissipative processes of the coupled cavity-vibration system, but shorter than the characteristic reaction times so that the initial reactant concentration is not significantly depleted, i.e., $1/\gamma_j \ll t_{\text{ss}} \ll (dN/dt)^{-1}$. For the urethane formation reaction, we take PHI as the reactive molecule and monitor the stationary intracavity occupation number $n_6 \equiv \langle \hat{b}_6^\dagger \hat{b}_6 \rangle_{\text{ss}}$ of the NCO (ν_6) vibrational mode, which is known to be involved in the formation of the activated complex outside the cavity [3], for all the molecules in the ensemble.

The rationale for the proposed cavity chemistry model builds on two physical assumptions: (1) chemical reactions only affect the vibrational sub-system of a coupled polaritonic state, i.e., *photons do not undergo chemistry*; (2) the population of reactive vibrational modes can increase or decrease the reaction probability depending on how it deviates from a thermal Boltzmann distribution. The first assumption motivates the local dissipation model used below to derive the equations of motion for the vibrational occupation number n_6 and photon-vibration coherences in the steady state. The second assumption rests on previous theory on the factors that affect the transmission coefficient $\kappa(T)$ in generalized formulation of transition state theory (TST) that accounts for quantum effects such as tunneling or internal level redistributions over chemically relevant timescales [52]. Specifically, it has been shown for gas-phase kinetics that internal-state nonequilibrium effects on the rate constant can be significant for bimolecular reactions with relatively low activation energies [53, 54, 55]. Extensions of these statistical theories to intracavity condensed-phase bimolecular reactions is subject of current work.

6.1 Single-Molecule Theory

We first focus on a single reactive molecule ($N = 1$) in an infrared resonator with a single quantized electromagnetic mode with bosonic field operator \hat{a} , resonant frequency ω_c and photon linewidth κ . We partition the total Hamiltonian of the coupled system as $\hat{H}_S = \hat{H}_0 + \hat{H}_c + \hat{V}$. The first term \hat{H}_0 is the vibrational Hamiltonian given in Eq. (S5), which encodes the free-space dynamics and spectrum of the ν_6 , ν_{14} and ν_{16} modes of the PHI molecule. The second term is the free cavity Hamiltonian $\hat{H}_c = \omega_k \sum_k \hat{a}_k^\dagger \hat{a}_k$, and the third term describes the molecule-cavity interaction in the rotating-wave approximation as

$$\hat{V} = \sum_k g_{6,k} (\hat{a}_k^\dagger \hat{b}_6 + \hat{a}_k \hat{b}_6^\dagger) + g_{F,k} (\hat{a}_k^\dagger \hat{b}_{14} \hat{b}_{16} + \hat{a}_k \hat{b}_{14}^\dagger \hat{b}_{16}^\dagger) \quad (\text{S10})$$

where we label cavity modes with the discrete label k . The Rabi frequencies for the ν_6 fundamental and the $\nu_{14} + \nu_{16}$ combination band of PHI in the k -th mode are $g_{6,k} \propto f_6$ and $g_{F,k} \propto f_{C3}$, with the transition dipoles f_6 and f_{C3} defined as in Eq. (S6). No external coherent driving terms are included in the Hamiltonian, to model a vacuum-only scenario. We consider a multi-mode picture for the cavity field to qualitatively capture the possible influence that moderately detuned modes in the cavity dispersion curve can have on the steady-state vibrational populations. The light-matter interaction model in Eq. (S10) can accurately reproduce linear and non-linear intracavity spectroscopy measurements [56], for the small coupling ratios $\Omega/\omega_c \sim 10^{-2}$ that are relevant in our problem.

We compute the evolution of the vibrational and cavity mode occupations for $N = 1$ by propagating a suitably chosen initial state $\hat{\rho}(0)$ up to the steady state with the quantum master equation

$$\dot{\hat{\rho}} = -i[\hat{H}_S, \hat{\rho}] + \mathcal{R}_\gamma[\hat{\rho}] + \mathcal{R}_\kappa[\hat{\rho}], \quad (\text{S11})$$

where \hat{H}_S is the total system Hamiltonian described above, \mathcal{R}_γ is the vibrational relaxation superoperator from Eq. (S8), and we now add a photonic relaxation superoperator given by

$$\mathcal{R}_\kappa[\hat{\rho}] = -\frac{\kappa}{2} \sum_k (n_c^{\text{th}} + 1) \left(\hat{a}_k^\dagger \hat{a}_k \hat{\rho} - 2\hat{a}_k \hat{\rho} \hat{a}_k^\dagger + \hat{\rho} \hat{a}_k^\dagger \hat{a}_k \right) - \frac{\kappa}{2} \sum_k n_c^{\text{th}} \left(\hat{a}_k \hat{a}_k^\dagger \hat{\rho} - 2\hat{a}_k^\dagger \hat{\rho} \hat{a}_k + \hat{\rho} \hat{a}_k \hat{a}_k^\dagger \right), \quad (\text{S12})$$

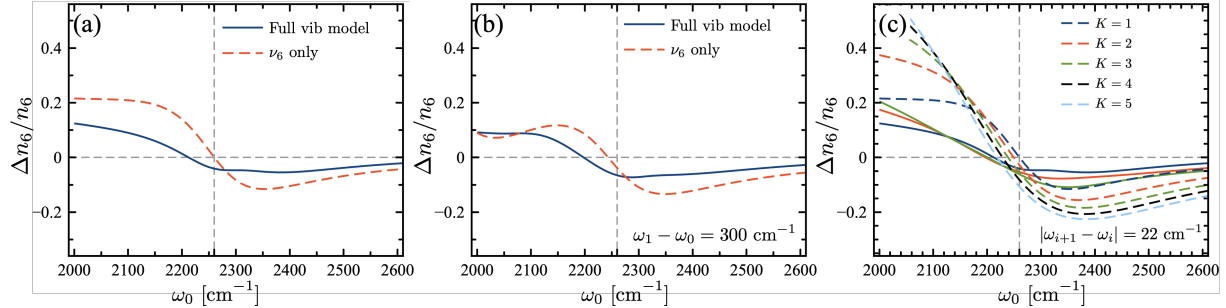


Figure S12: Deviations from the free-space thermal occupation at room temperature ($\Delta n_6/n_6$) for fundamental mode ν_6 at steady state as a function of cavity frequency ω_0 for the full vibrational model [Eq. (S5)] (solid lines) and a single molecular mode (dashed lines) under different cavity configurations. (a) Single cavity mode. (b) Two cavity modes considering $|\omega_0 - \omega_1| = 300 \text{ cm}^{-1}$. (c) From $K = 1$ up to $K = 5$ cavity modes taking $|\omega_i - \omega_j| = 22 \text{ cm}^{-1}$ with $|i - j| = 1$. All plots consider molecular parameters shown in Table S4 and photonic parameters $g_6 = 55 \text{ cm}^{-1}$, $g_F = (g_6/1.14)$ and $\kappa = 25 \text{ cm}^{-1}$.

where κ is a mode-independent photon decay rate and n_k^{th} is the thermal boson occupation of the k -th cavity mode. This form of the cavity dissipator ensures that the uncoupled cavity ($\hat{V} = 0$) equilibrates with the thermal background radiation at temperature T in steady state, for any initial conditions, i.e., $\langle \hat{a}_k^\dagger \hat{a}_k \rangle_{\text{ss}} = n_k^{\text{th}}$ for $t \gg \kappa^{-1}$. In the analysis below, we consider for numerical simplicity up to K cavity modes with a discrete set of frequencies $\{\omega_0, \omega_1, \dots, \omega_K\}$.

In Fig. S12 we solve for the steady-state vibrational occupation of the fundamental ν_6 mode for different coupling structures and cavity mode profiles. We quantify deviations from the free-space thermal occupation at room temperature by defining the ratio $\Delta n_6/n_6 \equiv (\langle \hat{b}_6^\dagger \hat{b}_6 \rangle_{\text{ss}} - n_6^{\text{th}})/n_6^{\text{th}}$, with $n_6^{\text{th}} = 1.9586 \times 10^{-5}$ at $T = 300 \text{ K}$. We check that our numerical calculations have enough numerical precision. The simplest case scenario is shown in S12a, where we consider a single molecule ($N = 1$) in a single-mode ($K = 1$) cavity field \hat{a}_0 , with resonant frequency ω_0 . The figure shows that when the cavity mode is resonant with the ν_6 fundamental (dashed vertical line), molecular models that ignore the Fermi coupling of ν_6 with the lower-frequency vibrations (ν_{14}, ν_{16}) predict $\Delta n_6 = 0$ for $\omega_0 = \omega_6$. On the contrary, when the Fermi resonance and the combination band are included in the vibrational Hamiltonian [see Eq. (S5)], there is a net cooling of the ν_6 mode on resonance. In both molecular vibration

models, the cavity induces an overall vibrational cooling effect ($\Delta n_6/n_6 \sim -0.1$) for cavity modes that are blue detuned relative to ν_6 . The cooling magnitude follows the vibrational absorption bandwidth (see Fig. S11, and for $(\omega_0 - \omega_6) \gg \gamma_6$, the effect vanishes. However, for red cavity detunings both vibrational models predict that an overall vibrational heating effect ($\Delta n_6/n_6 \sim +0.1$) can be expected, which persists over a broader range of single-mode cavity frequencies.

Realistic infrared cavities have a multi-mode character and therefore we study how the steady state ν_6 occupation is affected by the presence of additional photon modes ($K > 1$). First, we consider an idealized scenario where there are only two Lorentzian modes in the cavity spectrum, with one mode centered at ω_0 and the other mode locked in frequency at $\omega_1 = \omega_0 + 300 \text{ cm}^{-1}$. This case can be relevant to describe cavities with three-dimensional electromagnetic field confinement and a large free spectral range [57]. Figure S12b shows $\Delta n_6/n_6$ as a function of the lower mode frequency ω_0 for this two-mode scenario, keeping the frequency difference ($\omega_1 - \omega_0$) constant. Both vibrational Hamiltonian models (with and without Fermi coupling) predict a behavior that is qualitatively similar to the single-mode case (Fig. S12a), i.e., cooling on blue detuning and heating on red detuning, but the are quantitative differences, especially in red detuning.

6.2 Analytical Approximations

The single and two-mode results in Figs. S12a and S12b can be understood analytically for a vibrational model that neglects the Fermi resonance that gives rise to the combination band in the PHI spectrum. Starting from the quantum master equation [Eq. (S11)] with $g_F = \gamma_{14} = \gamma_{16} = 0$, we derive a linear system of equations for the quadratic moments

$\langle \hat{O}_1(t)\hat{O}_2(t) \rangle$ that reads

$$\frac{d}{dt}\langle \hat{b}_6^\dagger \hat{b}_6 \rangle = \gamma_6(n_6^{\text{th}} - \langle \hat{b}_6^\dagger \hat{b}_6 \rangle) - ig_{6,0}(\langle \hat{a}_0 \hat{b}_6^\dagger \rangle - \langle \hat{a}_0^\dagger \hat{b}_6 \rangle) - ig_{6,1}(\langle \hat{a}_1 \hat{b}_6^\dagger \rangle - \langle \hat{a}_1^\dagger \hat{b}_6 \rangle) \quad (\text{S13})$$

$$\frac{d}{dt}\langle \hat{a}_0^\dagger \hat{a}_0 \rangle = \kappa(n_0^{\text{th}} - \langle \hat{a}_0^\dagger \hat{a}_0 \rangle) - ig_{6,0}(\langle \hat{a}_0^\dagger \hat{b}_6 \rangle - \langle \hat{a}_0 \hat{b}_6^\dagger \rangle) \quad (\text{S14})$$

$$\frac{d}{dt}\langle \hat{a}_1^\dagger \hat{a}_1 \rangle = \kappa(n_1^{\text{th}} - \langle \hat{a}_1^\dagger \hat{a}_1 \rangle) - ig_{6,1}(\langle \hat{a}_1^\dagger \hat{b}_6 \rangle - \langle \hat{a}_1 \hat{b}_6^\dagger \rangle) \quad (\text{S15})$$

$$\frac{d}{dt}\langle \hat{a}_0 \hat{b}_6^\dagger \rangle = -(i\Delta_{0,6} + (\kappa + \gamma_6)/2)\langle \hat{a}_0 \hat{b}_6^\dagger \rangle + ig_{6,0}(\langle \hat{a}_0^\dagger \hat{a}_0 \rangle - \langle \hat{b}_6^\dagger \hat{b}_6 \rangle) \quad (\text{S16})$$

$$\frac{d}{dt}\langle \hat{a}_1 \hat{b}_6^\dagger \rangle = -(i\Delta_{1,6} + (\kappa + \gamma_6)/2)\langle \hat{a}_1 \hat{b}_6^\dagger \rangle + ig_{6,1}(\langle \hat{a}_1^\dagger \hat{a}_1 \rangle - \langle \hat{b}_6^\dagger \hat{b}_6 \rangle), \quad (\text{S17})$$

where $\Delta_{k,6} = \omega_k - \omega_6$ is the cavity detuning ($k = \{0, 1\}$). The steady state solutions $\langle \hat{O}_1 \hat{O}_2 \rangle_{\text{ss}}$ are obtained by setting the time derivatives to zero and solving the resulting system of algebraic equations. In particular, the complex steady-state photon-vibration coherence does not vanish under thermal equilibrium but can be written for the k -th mode as

$$\langle \hat{a}_k \hat{b}_6^\dagger \rangle_{\text{ss}} = \frac{-g_{6,k}(\langle \hat{b}_6^\dagger \hat{b}_6 \rangle_{\text{ss}} - \langle \hat{a}_k^\dagger \hat{a}_k \rangle_{\text{ss}})[\Delta_{k,6} + i(\kappa + \gamma_6)/2]}{(\kappa + \gamma_6)^2/4 + \Delta_{k,6}^2}. \quad (\text{S18})$$

Steady-state coherences are known to emerge for strongly coupled degrees of freedom in the absence of external coherent driving (e.g., lasers)[58, 59]. In terms of the light-matter coherence, the steady-state deviations of the vibrational and cavity mode occupation numbers can be written as

$$\langle \hat{b}_6^\dagger \hat{b}_6 \rangle_{\text{ss}} - n_6^{\text{th}} = -i \sum_k \frac{g_{6,k}}{\gamma_6} (\langle \hat{a}_k \hat{b}_6^\dagger \rangle_{\text{ss}} - \langle \hat{a}_k^\dagger \hat{b}_6 \rangle_{\text{ss}}) \quad (\text{S19})$$

$$\langle \hat{a}_k^\dagger \hat{a}_k \rangle_{\text{ss}} - n_k^{\text{th}} = -i \frac{g_{6,k}}{\kappa} (\langle \hat{a}_k^\dagger \hat{b}_6 \rangle - \langle \hat{a}_k \hat{b}_6^\dagger \rangle), \quad (\text{S20})$$

which show the direct influence of the Rabi frequency $g_{6,k}$ in the deviation from the uncoupled thermal occupations n_6^{th} and n_k^{th} at a given temperature T . Combining Eqs. (S19), (S20) and (S18), the stationary ν_6 occupation in the presence of two cavity modes ($K = 2$) can be written as

$$\langle \hat{b}_6^\dagger \hat{b}_6 \rangle_{\text{ss}} = n_6^{\text{th}} + \left[\frac{\kappa\alpha_0}{\kappa + \alpha_0} (n_0^{\text{th}} - n_6^{\text{th}}) + \frac{\kappa\alpha_1}{\kappa + \alpha_1} (n_1^{\text{th}} - n_6^{\text{th}}) \right] \left(\gamma_6 + \frac{\kappa\alpha_0}{\kappa + \alpha_0} + \frac{\kappa\alpha_1}{\kappa + \alpha_1} \right)^{-1}, \quad (\text{S21})$$

where the relevant light-matter coupling parameter is

$$\alpha_k = \frac{4g_{6,k}^2(\kappa + \gamma_6)}{(\kappa + \gamma_6)^2 + 4\Delta_{k,6}^2}. \quad (\text{S22})$$

The stationary cavity mode occupations are given by

$$\langle \hat{a}_0^\dagger \hat{a}_0 \rangle_{\text{ss}} = n_0^{\text{th}} - \left[\frac{\gamma_6 \alpha_0 (\kappa + \alpha_1) (n_0^{\text{th}} - n_6^{\text{th}})}{(\gamma_6 + \alpha_0)(\kappa + \alpha_1) + \kappa \alpha_1} + \frac{\kappa \alpha_0 \alpha_1 (n_0^{\text{th}} - n_1^{\text{th}})}{(\gamma_6 + \alpha_0)(\kappa + \alpha_1) + \kappa \alpha_1} \right] \times \left(\kappa + \frac{\alpha_0 [\gamma_6(\kappa + \alpha_1) + \kappa \alpha_1]}{(\gamma_6 + \alpha_0)(\kappa + \alpha_1) + \kappa \alpha_1} \right)^{-1} \quad (\text{S23})$$

$$\langle \hat{a}_1^\dagger \hat{a}_1 \rangle_{\text{ss}} = n_1^{\text{th}} - \left[\frac{\gamma_6 \alpha_1 (\kappa + \alpha_0) (n_1^{\text{th}} - n_6^{\text{th}})}{(\gamma_6 + \alpha_1)(\kappa + \alpha_0) + \kappa \alpha_0} + \frac{\kappa \alpha_1 \alpha_0 (n_1^{\text{th}} - n_0^{\text{th}})}{(\gamma_6 + \alpha_1)(\kappa + \alpha_0) + \kappa \alpha_0} \right] \times \left(\kappa + \frac{\alpha_1 [\gamma_6(\kappa + \alpha_0) + \kappa \alpha_0]}{(\gamma_6 + \alpha_1)(\kappa + \alpha_0) + \kappa \alpha_0} \right)^{-1}. \quad (\text{S24})$$

Equations (S21), (S23) and (S24) reduce to well-defined free-space thermal equilibrium values in the limit where light-matter interaction is negligible ($\alpha_k \rightarrow 0$). The theory also shows that for a cavity mode that is on exact resonance with the ν_6 fundamental ($\Delta_{k,6} = 0$), the bare thermal occupations become identical ($n_k^{\text{th}} = n_6^{\text{th}}$) and there is no contribution of that mode to the overall heating or cooling effect. This agrees with the numerical results in Figs. S12a and S12b for the vibrational model without Fermi coupling (ν_6 -only), i.e., for a single mode ω_0 there no effect on exact resonance (Fig. S12a), but the presence of a second blue-detuned mode ω_1 leads to cooling on resonance (Fig. S12b).

For large positive or negative cavity detunings, we can assume the following frequency hierarchy: $\Delta_{k,6} \gg g_{k,6} > \kappa \sim \gamma_6$. Under these conditions, we can define the small parameters $x_k \equiv \alpha_k/\kappa \ll 1$ and $y_k \equiv \alpha_k/\gamma_6 \ll 1$ and write the steady-state far off-resonance ν_6 occupation as $\langle \hat{b}_6^\dagger \hat{b}_6 \rangle_{\text{ss}} \approx n_6^{\text{th}} + y_0(n_0^{\text{th}} - n_6^{\text{th}}) + y_1(n_1^{\text{th}} - n_6^{\text{th}})$, to lowest order in x_k and y_k . Further writing the thermal occupation of the cavity modes as $n_k^{\text{th}} = (\exp[(\omega_k + \Delta_{k,6})/k_B T] - 1)^{-1}$ gives an expression for $\Delta n_6/n_6$ in the dispersive limit that reads

$$\frac{\Delta n_6}{n_6} \approx \frac{g_{6,0}^2}{\Delta_{0,6}^2} (1 + \kappa/\gamma_6) (e^{-\Delta_{0,6}/k_B T} - 1) + \frac{g_{6,1}^2}{\Delta_{1,6}^2} (1 + \kappa/\gamma_6) (e^{-\Delta_{1,6}/k_B T} - 1), \quad (\text{S25})$$

which is consistent with the numerical results in Figs. S12a and S12b, when both ω_0 and ω_1 are far off-resonance from the ν_6 fundamental.

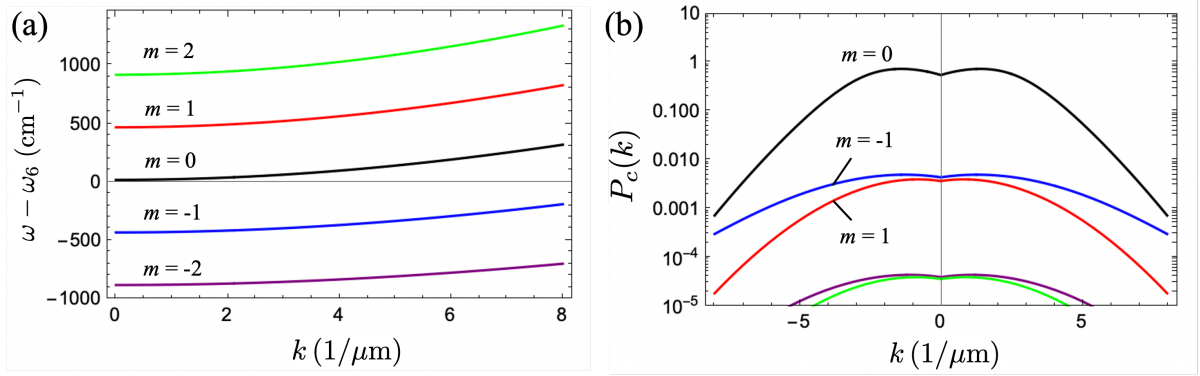


Figure S13: (a) Model cavity frequency dispersion $\omega_m(k)$ for 5 discrete photon resonances with mode order m . The central mode $m = 0$ is near resonant with the NCO vibrational frequency $\omega_6 \approx 2280 \text{ cm}^{-1}$ at normal incidence ($k = 0$); (b) Probability density $P_c(k)$ from Eq. (S28) corresponding to each photonic resonance mode in panel (a).

The two-mode expression in Eq. (S21) highlights the additive character of the contribution per mode, which could be either constructive or destructive depending on the detuning of each mode relative to ω_6 . For example, the dip in the ratio $\Delta n_6/n_6$ near 2025 cm^{-1} in Fig. S12b occurs because while the lower cavity mode ω_0 gives a net heating effect ($n_0^{\text{th}} > n_6^{\text{th}}$), the higher mode ω_1 around 2325 cm^{-1} is blue-detuned from the ν_6 vibration and therefore gives net cooling ($n_1^{\text{th}} < n_6^{\text{th}}$). Extrapolating this additive behavior to a finite but possibly large number of discrete modes K , we conjecture a generalization of Eq. (S21) for multi-mode cavities of the form

$$\langle \hat{b}_6^\dagger \hat{b}_6 \rangle_{\text{ss}} = n_6^{\text{th}} + \frac{\sum_{k=0}^{K-1} \frac{\kappa \alpha_k}{\kappa + \alpha_k} [n_k^{\text{th}} - n_6^{\text{th}}]}{\gamma_6 + \sum_{k=0}^{K-1} \frac{\kappa \alpha_k}{\kappa + \alpha_k}}, \quad (\text{S26})$$

where α_k and n_k^{th} depend on the mode detuning $\Delta_{k,6}$. We therefore expect an overall vibrational cooling effect for closely spaced cavity modes that are predominantly blue detuned from the ν_6 fundamental and an overall vibrational heating for modes that are predominantly red detuned.

This is confirmed numerically in Fig. S12c, with up to $K = 5$ modes that equally spaced by 22 cm^{-1} in order of increasing frequency, with ω_0 being the lowest energy mode. The results clearly show that the magnitude of the deviation $\Delta n_6/n_6$ increases monotonically with the number of modes included in the calculation, for both vibrational models with and without

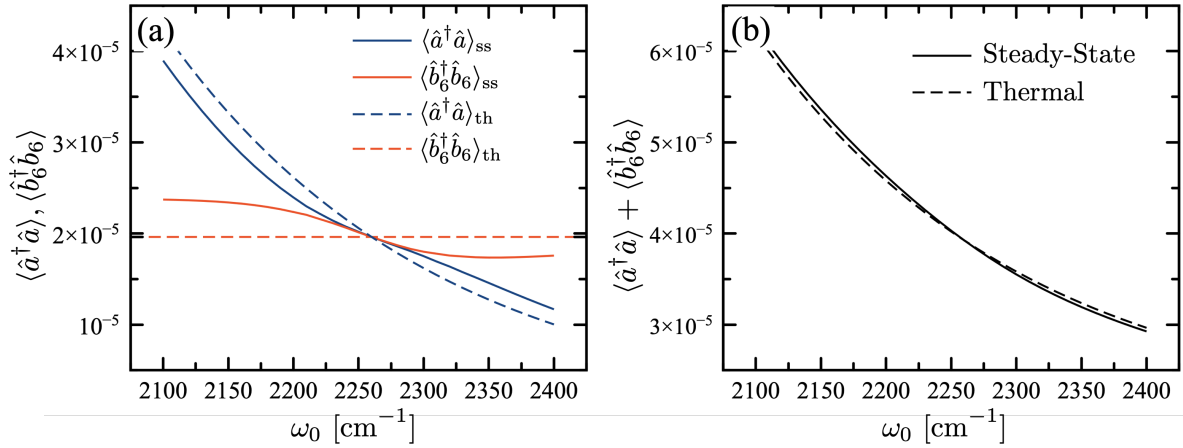


Figure S14: Vibrational and cavity stationary occupation numbers as a function of the cavity resonance frequency ω_0 . (a) Occupation of fundamental vibrational mode \hat{b}_6 (solid blue) and the cavity mode \hat{a} (solid red) for a single-mode cavity. Dashed lines correspond to the bare thermal occupation numbers. (b) Total stationary occupation number ($\langle \hat{b}_6^\dagger \hat{b}_6 \rangle_{\text{ss}} + \langle \hat{a}^\dagger \hat{a} \rangle_{\text{ss}}$) versus total bare thermal occupation ($n_6^{\text{th}} + \sum_k n_0^{\text{th}}$), for the system parameters used in Fig. S12a.

Fermi coupling physics. To treat an entire dispersion curve, we can rewrite Eq. (S26) by introducing a k -dependence to the photon decay rate, i.e., $\kappa \rightarrow \kappa_k$, approximating the Bose occupation numbers by Boltzmann factors as in Eq. (S25) to obtain

$$\frac{\Delta n_6}{n_6} \approx \sum_k P_c(k) \left(e^{-\Delta_{k,6}/k_B T} - 1 \right) \left(1 - \gamma_6/\mathcal{N}_c \right), \quad (\text{S27})$$

which is a weighted average of the relative cavity and vibrational occupations determined by the cavity-dependent probability density

$$P_c(k) = \frac{1}{\mathcal{N}_c} \left(\frac{\kappa_k \alpha_k}{\kappa_k + \alpha_k} \right), \quad (\text{S28})$$

with α_k given in Eq. (S22) and normalization factor given by $\mathcal{N}_c \equiv \sum_k \kappa_k \alpha_k / (\kappa_k + \alpha_k)$ in units of frequency. The leading term from Eq. (S27) is Eq. 2 in the main text ($\mathcal{N}_c > \gamma_6$).

For concreteness, in Fig. 3a of the main text, we used Eq. (S27) to compute the vibrational occupation deviation $\Delta n_6/n_6$ associated with a realistic photonic structure that has a multi-mode spectrum $\omega_n(k)$ that closely resembles the experimental dispersion curves in Fig. S5d, which have a resonant mode at normal incidence ($k = 0$) with the NCO vibrational mode ν_6 .

Figure S13a shows the bare dispersion curves included in the calculation, with one mode being resonant with ω_6 at $k = 0$ and neighboring modes separated by a free spectral range of ≈ 480 cm^{-1} . As expected, Fig. S13b confirms that the resonant $m = 0$ mode at normal incidence gives the largest contribution to the sum-over-modes expression for $\Delta n_6/n_6$.

As a validity test of the model, in Fig. S14a we solve for the steady-state photon numbers $\langle \hat{a}_k^\dagger \hat{a}_k \rangle$ to confirm that the coupled light-matter system remains in thermal equilibrium with their bosonic reservoirs at temperature T , independent of the Rabi frequencies and cavity detunings, i.e., $\langle \hat{b}_6^\dagger \hat{b}_6 \rangle_{\text{ss}} + \sum_k \langle \hat{a}_k^\dagger \hat{a}_k \rangle_{\text{ss}} = n_6^{\text{th}} + \sum_k n_k^{\text{th}}$. From Eqs. (S19) and (S20), we expect exact conservation of the total thermal occupation at all frequencies for a single-mode cavity, as long as the vibrational and cavity resonances have the same bandwidth, i.e., $\gamma_6 = \kappa$. Figure S14b shows that for a finite bandwidth mismatch ($|\gamma_6 - \kappa| \approx 5 \text{ cm}^{-1}$ in Fig. S14), it is the frequency-integrated total bare occupation number what is conserved. This conservation of the total bare thermal occupation number implies that an external observer would not detect a net change in temperature of the coupled system relative to an uncoupled case. In other words, the predicted coupling-induced population redistribution between photonic and vibrational degrees of freedom would not be observable in global temperature measurements.

6.3 Redfield Quantum Master Equation in the Polariton Basis

For completeness, here we go one step beyond the Lindblad quantum master equation to solve for the reduced vibrational occupation of a single vibrational mode coupled to a single-mode cavity field in contact with a thermal bath at $T = 300$ K. From the quantum Liouville equation in the interaction picture with respect to a system-reservoir interaction Hamiltonian of the form $\hat{H}_{SB} = \hat{\mathcal{O}} \otimes \hat{\mathcal{B}}$, where the operator $\hat{\mathcal{O}}$ acts on the vibration-cavity system and $\hat{\mathcal{B}}$ is a bath operator, one can derive a Redfield quantum master equation for the system density matrix $\hat{\rho}$, which can be written as [60]

$$\dot{\hat{\rho}} = -i[\hat{H}_S, \hat{\rho}] + \tilde{\mathcal{R}}_{\gamma_6}[\hat{\rho}] + \tilde{\mathcal{R}}_{\kappa}[\hat{\rho}] + \tilde{\mathcal{D}}_{\phi_6}[\hat{\rho}] + \tilde{\mathcal{D}}_{\phi_c}[\hat{\rho}], \quad (\text{S29})$$

where the system Hamiltonian \hat{H}_S is the same used in Sec. 6.2. The incoherent energy exchange of the coupled light-matter system with the thermal bath is described by the combined action of the vibrational dissipator

$$\begin{aligned}\tilde{\mathcal{R}}_{6\alpha}[\hat{\rho}] = & \frac{1}{2} \left(\hat{b}_{6\alpha}^\dagger \hat{\rho} \hat{\mathcal{P}}_{6\alpha} + \hat{\mathcal{P}}_{6\alpha}^\dagger \hat{\rho} \hat{b}_{6\alpha} - \hat{b}_{6\alpha} \hat{\mathcal{P}}_{6\alpha}^\dagger \hat{\rho} - \hat{\rho} \hat{\mathcal{P}}_{6\alpha} \hat{b}_{6\alpha}^\dagger \right) \\ & + \frac{1}{2} \left(\hat{b}_{6\alpha} \hat{\rho} \hat{\mathcal{Q}}_{6\alpha}^\dagger + \hat{\mathcal{Q}}_{6\alpha}^\dagger \hat{\rho} \hat{b}_{6\alpha}^\dagger - \hat{b}_{6\alpha}^\dagger \hat{\mathcal{Q}}_{6\alpha} \hat{\rho} - \hat{\rho} \hat{\mathcal{Q}}_{6\alpha}^\dagger \hat{b}_{6\alpha} \right),\end{aligned}\quad (\text{S30})$$

and the photonic dissipator

$$\begin{aligned}\tilde{\mathcal{R}}_\kappa[\hat{\rho}] = & \frac{1}{2} \left(\hat{a}^\dagger \hat{\rho} \hat{\mathcal{P}}_\kappa + \hat{\mathcal{P}}_\kappa^\dagger \hat{\rho} \hat{a} - \hat{a} \hat{\mathcal{P}}_\kappa^\dagger \hat{\rho} - \hat{\rho} \hat{\mathcal{P}}_\kappa \hat{a}^\dagger \right) \\ & + \frac{1}{2} \left(\hat{a} \hat{\rho} \hat{\mathcal{Q}}_\kappa^\dagger + \hat{\mathcal{Q}}_\kappa^\dagger \hat{\rho} \hat{a}^\dagger - \hat{a}^\dagger \hat{\mathcal{Q}}_\kappa \hat{\rho} - \hat{\rho} \hat{\mathcal{Q}}_\kappa^\dagger \hat{a} \right).\end{aligned}\quad (\text{S31})$$

The operators $\hat{\mathcal{P}}$ and $\hat{\mathcal{Q}}$ respectively describe the absorption and of energy quanta from the reservoir and the emission of quanta into the reservoir, both processes being related by detailed balance [60]. They can be written in compact notation in terms of the polaritonic eigenstates $|\epsilon\rangle$ as

$$\hat{\mathcal{P}}_\Gamma = \Gamma \sum_{\epsilon, \epsilon'} \langle \epsilon' | \hat{O} | \epsilon \rangle n_{\epsilon, \epsilon'} |\epsilon'\rangle \langle \epsilon| \text{ and } \hat{\mathcal{Q}}_\Gamma = \Gamma \sum_{\epsilon, \epsilon'} \langle \epsilon' | \hat{O} | \epsilon \rangle (1 + n_{\epsilon, \epsilon'}) |\epsilon'\rangle \langle \epsilon|, \quad (\text{S32})$$

where $\{|\epsilon\rangle\}$ satisfies $\hat{H}_S |\epsilon\rangle = \omega_\epsilon |\epsilon\rangle$, and the rate $\Gamma = \kappa$ for photonic relaxation and $\Gamma = \gamma_6$ for vibrational relaxation. The corresponding system operators are $\hat{O} = \hat{a}$ for photons and $\hat{O} = \hat{b}_{6\alpha}$ for vibrations. We neglect bath-induced Lamb shifts and ignore the frequency dependence of the bare decay rates κ and γ_6 .

The Redfield tensor in Eq. (S29) also considers pure dephasing terms that can be written in the generic form

$$\tilde{\mathcal{D}}_\phi[\hat{\rho}] = -(\kappa_{\phi_j}/2)(\hat{O}^\dagger \hat{O} \hat{\rho} - 2\hat{O} \hat{\rho} \hat{O}^\dagger + \hat{\rho} \hat{O}^\dagger \hat{O}) \quad (\text{S33})$$

where $\hat{O}_d = \hat{b}_{6\alpha}^\dagger \hat{b}_{6\alpha}$ for pure vibrational dephasing at the rate κ_{ϕ_6} and $\hat{O}_d = \hat{a}^\dagger \hat{a}$ for pure photon dephasing at the rate κ_{ϕ_c} . These dephasing operators independently commute with the system Hamiltonian \hat{H}_S only for vanishing light-matter coupling. In the polariton eigenbasis $|\epsilon\rangle$, dephasing contributes to the dissipative mixing of vibrational polaritons. However, the

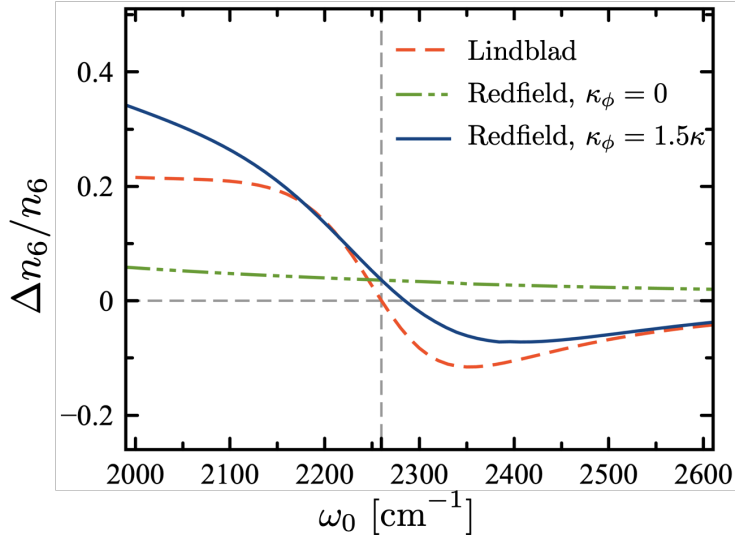


Figure S15: Deviations from the free-space thermal occupation at room temperature ($\Delta n_6/n_6$) for fundamental mode ν_6 at steady state as a function of cavity frequency ω_c for the Hamiltonian system \hat{H}_S subject to Redfield dissipative dynamics with $\kappa_\phi = \gamma_{6\phi} = 0$ (green dashed-dotted line), Redfield dissipative dynamics with $\kappa_\phi = \gamma_{6\phi} = 1.5\kappa$ (blue solid line) and Lindblad dynamics (red dashed line).

phase noise rates κ_ϕ are not bound limited by detailed balance because there is no energy exchange with the reservoir. For the uncoupled case ($g_{6\alpha} = 0$) and zero dephasing, Eq. (S29) reduces to the Lindblad form with local dissipation given by Eq. (S11). The Redfield tensor in the polaritonic basis $|\epsilon\rangle$ therefore introduces collective incoherent processes that are otherwise absent in the local Lindblad description discussed in Sec. 6.2.

6.3.1 Canonical Thermal versus non-Canonical Steady States

Figure S15 shows the stationary deviation of the vibrational occupation $\Delta n_6/n_6$ as a function of the cavity frequency ω_c , for a. single molecule coupled to a single-mode cavity with the same system Hamiltonian but different relaxation models. We compare the steady-state of the Lindblad quantum master equation [Eq. (S11)] (red dashed line) and the Redfield equation [Eq. (S29)] with (blue solid line) and without (green dashed-dotted line) pure dephasing contributions. While the Redfield model in the polaritonic basis without pure dephasing

does not predict a resonant feature in the frequency-dependence of the vibrational occupation number, adding pure dephasing terms results in a cavity frequency dependence similar to Lindblad model predictions in Fig. S12a.

As a consequence of detailed balance, the steady-state solution of the Redfield quantum master equation is the canonical thermal (Boltzmann) state [60]

$$\hat{\rho}_S^{\text{th}} = \frac{e^{-\beta \hat{H}_S}}{\mathcal{Z}}, \quad (\text{S34})$$

where \hat{H}_S is the coupled system Hamiltonian, $\mathcal{Z} = \text{Tr}[e^{-\beta \hat{H}_S}]$ is the partition function and $\beta = 1/k_B T$. Figure S15 therefore suggests that the existence of narrow features in the frequency dependence of the vibrational occupation number $\langle \hat{b}_6^\dagger \hat{b}_6 \rangle$ implies that the reduced light-matter system deviates from the canonical Boltzmann state in Eq. (S34) in the steady state. Deviations from the canonical state can be expected for the strong dephasing conditions assumed in Fig. S15 [38]. In other words, the local Lindblad theory adopted to derive the equations in Sec. 6.2 for $N = 1$ and to obtain the results in Fig. 3 from the main text implicitly neglects vibrational and photonic coherences that are otherwise embedded in a polaritonic thermal state $\hat{\rho}_S^{\text{th}} = \mathcal{Z}^{-1} \exp^{-\beta \sum_\epsilon \omega_\epsilon |\epsilon\rangle\langle\epsilon|}$. The fact that polaritonic Boltzmann states do not lead to narrow resonant features of the vibrational occupation number as a function of detuning may stimulate further research on the nature of thermalization in strongly coupled light-matter systems and its implications for intracavity chemistry. Recent progress in this direction has been studied in the context of circuit QED by calculating genuinely quantum correlations between light and matter in thermal states of the Rabi model, through the quantum discord [61].

6.3.2 Spectroscopic Equivalence of Lindblad and Redfield Models

In order to check the consistency of the theoretical models with experimental measurements, we calculate the absorption spectrum $\mathcal{A}(\omega_d)$ of a cavity mode on resonant with a single molecule as function of the laser frequency ω_d . We consider that the cavity is driven by a cw laser. In this form, the total Hamiltonian is given by $\hat{H}(t) = \hat{H}_S + \tilde{V}(t)$, where \hat{H}_S is the cavity-molecule Hamiltonian used in Eq. (S29) and $\tilde{V}(t) = f_0(\hat{a}e^{i\omega_d t} + \hat{a}^\dagger e^{-i\omega_d t})$ with $f_0 \ll \kappa$ (weak driving).

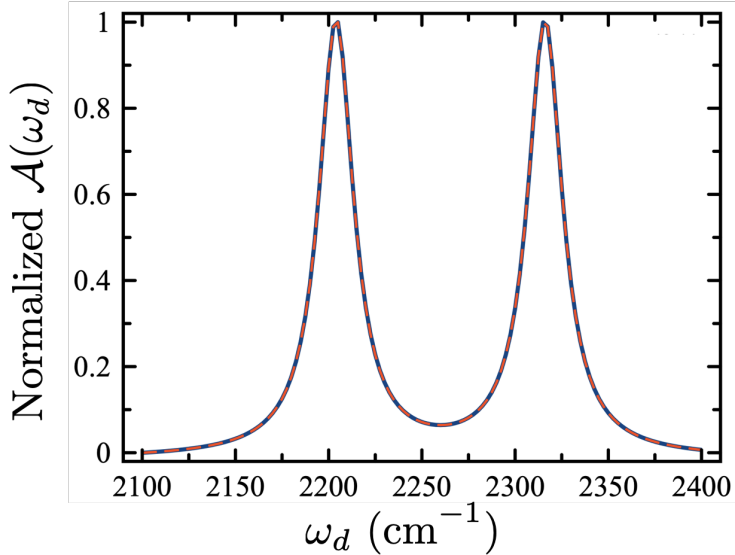


Figure S16: Infrared absorption spectrum of a single molecule on resonance with a cavity mode as a function of laser frequency ω_d by solving the Redfield (solid line) and Lindblad (dashed line) quantum master equation. Peaks represent the well known lower and upper polaritons in strong light-matter coupling regime and the energy difference between peaks corresponds to Rabi splitting ($\Omega \approx 112 \text{ cm}^{-1}$).

Figure S16 shows the absorption spectrum calculated with the Lindblad [Eq. (S11)] and Redfield [Eq. (S29)] open quantum system models. For the Redfield model, we set $\kappa_\phi = \gamma_\phi = 0$ to ensure that the laser-free steady state has canonical Boltzmann form. Our results show that although the Lindblad and Redfield theories can give qualitatively different predictions for the cavity-frequency dependence of the vibrational occupation number (see Fig. S15), they predict the same linear transmission spectrum.

In what follows, we restrict our discussion to the Lindblad open quantum system model, which was used to obtain the results in Fig. 3 of the main text.

6.4 Many-body cavity chemistry

6.4.1 Truncated equations of motion including Fermi resonance

We are interested in capturing the influence of the Fermi resonance between the ν_6 fundamental and the combination band $\nu_{14} + \nu_{16}$ on the steady state occupation numbers $\langle \hat{b}_{6\alpha}^\dagger \hat{b}_{6\alpha} \rangle$ of

the α -th species in an ensemble of N molecules. To simplify the numerical scaling of the many-body solutions, we factorize local third-order photon-vibration correlations as $\langle \hat{a}^\dagger \hat{b}_{j_\alpha} \hat{b}_{k_\alpha} \rangle \approx \langle \hat{a}^\dagger \rangle \langle \hat{b}_{j_\alpha} \hat{b}_{k_\alpha} \rangle$. Similarly, local mode-mode vibrational correlations are factorized as $\langle \hat{b}_{6_\alpha}^\dagger \hat{b}_{j_\alpha} \hat{b}_{k_\alpha} \rangle \approx \langle \hat{b}_{6_\alpha}^\dagger \rangle \langle \hat{b}_{j_\alpha} \hat{b}_{k_\alpha} \rangle$, $\langle \hat{b}_{j_\alpha} \hat{b}_{k_\alpha}^\dagger \rangle \approx \langle \hat{b}_{k_\alpha}^\dagger \hat{b}_{j_\alpha} \rangle$ for $j \neq k$, and $\langle \hat{b}_{j_\alpha} \hat{b}_{k_\alpha} \rangle \approx \langle \hat{b}_{k_\alpha} \hat{b}_{j_\alpha} \rangle$ for $j \neq k$. More sophisticated factorization schemes based on cumulant expansions are also possible [58, 62].

The many-particle system Hamiltonian \hat{H}_S that is used to solve the quantum master equation is a straightforward generalization of the $N = 1$ vibrational model with Fermi coupling from Sec. 6.1. Assuming for simplicity that the cavity has a single mode at frequency ω_0 (linewidth κ), we partition the Hamiltonian as

$$\hat{H}_S = \omega_c \hat{a}^\dagger \hat{a} + \sum_{\alpha=1}^N \hat{H}_{0\alpha} + \sum_{\alpha=1}^N \hat{V}_\alpha, \quad (\text{S35})$$

with a local vibrational Hamiltonian given by

$$\hat{H}_{0\alpha} = \omega_{6\alpha} \hat{b}_{6_\alpha}^\dagger \hat{b}_{6_\alpha} + \sum_{j=14,16} \omega_j \hat{b}_{j_\alpha}^\dagger \hat{b}_{j_\alpha} + \lambda \left(\hat{b}_{14_\alpha}^\dagger \hat{b}_{16_\alpha} + \hat{b}_{14_\alpha} \hat{b}_{16_\alpha}^\dagger \right) + \sum_{j=14,16} \zeta_j \left(\hat{b}_{6_\alpha}^\dagger \hat{b}_{j_\alpha} \hat{b}_{j_\alpha} + \hat{b}_{6_\alpha} \hat{b}_{j_\alpha}^\dagger \hat{b}_{j_\alpha}^\dagger \right), \quad (\text{S36})$$

and local cavity-vibration coupling of the form

$$\hat{V}_\alpha = g_6 \left(\hat{a}^\dagger \hat{b}_{6_\alpha} + \hat{a} \hat{b}_{6_\alpha}^\dagger \right) + g_F \left(\hat{a}^\dagger \hat{b}_{14_\alpha} \hat{b}_{16_\alpha} + \hat{a} \hat{b}_{14_\alpha}^\dagger \hat{b}_{16_\alpha}^\dagger \right). \quad (\text{S37})$$

The many-body quantum master equation simply extends the one-particle case, i.e.,

$$\dot{\hat{\rho}} = -i[\hat{H}_S, \hat{\rho}] + \sum_{\alpha=1}^N \mathcal{R}_{\gamma\alpha}[\hat{\rho}] + \mathcal{R}_\kappa[\hat{\rho}], \quad (\text{S38})$$

with \hat{H}_S given by Eq. (S35) and $\mathcal{R}_\kappa[\hat{\rho}]$ in Eq. (S12). For simplicity, we assume that each molecule is only subject to a local intramolecular vibrational reservoir $\mathcal{R}_{\gamma\alpha}$, given by Eq. (S8). More complicated reservoir models with site off-diagonal dissipators in principle can also be taken into account [58].

From the quantum master equation we can derive a system of coupled nonlinear equations for first moments $\langle \hat{O}_1 \rangle = \text{tr}[\hat{O}_1 \hat{\rho}]$ and second moments $\langle \hat{O}_1 \hat{O}_2 \rangle = \text{tr}[\hat{O}_1 \hat{O}_2 \hat{\rho}]$, where \hat{O}_1 and

\hat{O}_2 represent either photonic or vibrational mode operators. The nonlinearity arises from the truncation of third order correlations. Two-time correlation functions $\langle \hat{O}_1(t) \hat{O}_2(t + \tau) \rangle$ can be related to equal-time dynamical variables via quantum regression formulas [63]. Using Eqs. (S38), (S35), (S8) and (S12), we obtain the following system of equations

$$\begin{aligned} \frac{d}{dt} \langle \hat{a}^\dagger \hat{a} \rangle = & \kappa (n_c^{\text{th}} - \langle \hat{a}^\dagger \hat{a} \rangle) - ig_6 \sum_{\alpha} \left(\langle \hat{a} \hat{b}_{6\alpha}^\dagger \rangle^* - \langle \hat{a} \hat{b}_{6\alpha}^\dagger \rangle \right) \\ & - ig_F \sum_{\alpha} \left(\langle \hat{a} \rangle^* \langle \hat{b}_{16\alpha} \hat{b}_{14\alpha} \rangle - \langle \hat{a} \rangle \langle \hat{b}_{16\alpha} \hat{b}_{14\alpha} \rangle^* \right) \end{aligned} \quad (\text{S39})$$

$$\frac{d}{dt} \langle \hat{a} \rangle = -(\kappa/2 + i\omega_c) \langle \hat{a} \rangle - i \sum_{\alpha} \left(g_6 \langle \hat{b}_{6\alpha} \rangle + g_F \langle \hat{b}_{16\alpha} \hat{b}_{14\alpha} \rangle \right) \quad (\text{S40})$$

$$\frac{d}{dt} \langle \hat{b}_{6\alpha} \rangle = -(\gamma_6/2 + i\omega_6) \langle \hat{b}_{6\alpha} \rangle - ig_6 \langle \hat{a} \rangle - i\zeta_{14} \langle \hat{b}_{14\alpha} \hat{b}_{14\alpha} \rangle - i\zeta_{16} \langle \hat{b}_{16\alpha} \hat{b}_{16\alpha} \rangle \quad (\text{S41})$$

$$\begin{aligned} \frac{d}{dt} \langle \hat{a} \hat{b}_{6\alpha}^\dagger \rangle = & -[(\kappa + \gamma_6)/2 + i(\omega_c - \omega_6)] \langle \hat{a} \hat{b}_{6\alpha}^\dagger \rangle + i \langle \hat{a} \rangle \left(\zeta_{14} \langle \hat{b}_{14\alpha} \hat{b}_{14\alpha} \rangle^* + \zeta_{16} \langle \hat{b}_{16\alpha} \hat{b}_{16\alpha} \rangle^* \right) \\ & + ig_6 (\langle \hat{a}^\dagger \hat{a} \rangle - \langle \hat{b}_{6\alpha}^\dagger \hat{b}_{6\alpha} \rangle) - ig_F \langle \hat{b}_{6\alpha} \rangle^* \langle \hat{b}_{16\alpha} \hat{b}_{14\alpha} \rangle \end{aligned} \quad (\text{S42})$$

$$\begin{aligned} \frac{d}{dt} \langle \hat{b}_{6\alpha}^\dagger \hat{b}_{6\alpha} \rangle = & \gamma_6 \left(n_6 - \langle \hat{b}_{6\alpha}^\dagger \hat{b}_{6\alpha} \rangle \right) - i\zeta_{14} \left(\langle \hat{b}_{6\alpha} \rangle^* \langle \hat{b}_{14\alpha} \hat{b}_{14\alpha} \rangle - \langle \hat{b}_{6\alpha} \rangle \langle \hat{b}_{14\alpha} \hat{b}_{14\alpha} \rangle^* \right) \\ & - ig_6 \left(\langle \hat{a} \hat{b}_{6\alpha}^\dagger \rangle - \langle \hat{a} \hat{b}_{6\alpha}^\dagger \rangle^* \right) - i\zeta_{16} \left(\langle \hat{b}_{6\alpha} \rangle^* \langle \hat{b}_{16\alpha} \hat{b}_{16\alpha} \rangle - \langle \hat{b}_{6\alpha} \rangle \langle \hat{b}_{16\alpha} \hat{b}_{16\alpha} \rangle^* \right) \end{aligned} \quad (\text{S43})$$

$$\begin{aligned} \frac{d}{dt} \langle \hat{b}_{14\alpha}^\dagger \hat{b}_{14\alpha} \rangle = & \gamma_{14} \left(n_{14} - \langle \hat{b}_{14\alpha}^\dagger \hat{b}_{14\alpha} \rangle \right) - 2i\zeta_{14} \left(\langle \hat{b}_{6\alpha} \rangle \langle \hat{b}_{14\alpha} \hat{b}_{14\alpha} \rangle^* - \langle \hat{b}_{6\alpha} \rangle^* \langle \hat{b}_{14\alpha} \hat{b}_{14\alpha} \rangle \right) \\ & + i\lambda \left(\langle \hat{b}_{16\alpha}^\dagger \hat{b}_{14\alpha} \rangle - \langle \hat{b}_{16\alpha}^\dagger \hat{b}_{14\alpha} \rangle^* \right) - ig_F \left(\langle \hat{a} \rangle \langle \hat{b}_{16\alpha} \hat{b}_{14\alpha} \rangle^* - \langle \hat{a} \rangle^* \langle \hat{b}_{16\alpha} \hat{b}_{14\alpha} \rangle \right) \end{aligned} \quad (\text{S44})$$

$$\begin{aligned} \frac{d}{dt} \langle \hat{b}_{16\alpha}^\dagger \hat{b}_{16\alpha} \rangle = & \gamma_{16} \left(n_{16} - \langle \hat{b}_{16\alpha}^\dagger \hat{b}_{16\alpha} \rangle \right) - 2i\zeta_{16} \left(\langle \hat{b}_{6\alpha} \rangle \langle \hat{b}_{16\alpha} \hat{b}_{16\alpha} \rangle^* - \langle \hat{b}_{6\alpha} \rangle^* \langle \hat{b}_{16\alpha} \hat{b}_{16\alpha} \rangle \right) \\ & - i\lambda \left(\langle \hat{b}_{16\alpha}^\dagger \hat{b}_{14\alpha} \rangle - \langle \hat{b}_{16\alpha}^\dagger \hat{b}_{14\alpha} \rangle^* \right) - ig_F \left(\langle \hat{a} \rangle \langle \hat{b}_{16\alpha} \hat{b}_{14\alpha} \rangle^* - \langle \hat{a} \rangle^* \langle \hat{b}_{16\alpha} \hat{b}_{14\alpha} \rangle \right) \end{aligned} \quad (\text{S45})$$

$$\begin{aligned} \frac{d}{dt} \langle \hat{b}_{14\alpha} \hat{b}_{14\alpha} \rangle = & -(\gamma_{14} + 2i\omega_{14}) \langle \hat{b}_{14\alpha} \hat{b}_{14\alpha} \rangle - 2i\lambda \langle \hat{b}_{16\alpha} \hat{b}_{14\alpha} \rangle \\ & - 2i\zeta_{14} \langle \hat{b}_{6\alpha} \rangle \left(1 + 2 \langle \hat{b}_{14\alpha}^\dagger \hat{b}_{14\alpha} \rangle \right) - 2ig_F \langle \hat{a} \rangle \langle \hat{b}_{16\alpha}^\dagger \hat{b}_{14\alpha} \rangle \end{aligned} \quad (\text{S46})$$

$$\begin{aligned} \frac{d}{dt} \langle \hat{b}_{16\alpha} \hat{b}_{16\alpha} \rangle &= -(\gamma_{16} + 2i\omega_{16}) \langle \hat{b}_{16\alpha} \hat{b}_{16\alpha} \rangle - 2i\lambda \langle \hat{b}_{16\alpha} \hat{b}_{14\alpha} \rangle \\ &\quad - 2i\zeta_{16} \langle \hat{b}_{6\alpha} \rangle \left(1 + 2 \langle \hat{b}_{16\alpha}^\dagger \hat{b}_{16\alpha} \rangle \right) - 2ig_F \langle \hat{a} \rangle \langle \hat{b}_{16\alpha}^\dagger \hat{b}_{14\alpha} \rangle^* \end{aligned} \quad (\text{S47})$$

$$\begin{aligned} \frac{d}{dt} \langle \hat{b}_{16\alpha} \hat{b}_{14\alpha} \rangle &= -((\gamma_{14} + \gamma_{16})/2 + i(\omega_{14} + \omega_{16})) \langle \hat{b}_{16\alpha} \hat{b}_{14\alpha} \rangle - i\lambda \left(\langle \hat{b}_{14\alpha} \hat{b}_{14\alpha} \rangle + \langle \hat{b}_{16\alpha} \hat{b}_{16\alpha} \rangle \right) \\ &\quad - 2i \langle \hat{b}_{6\alpha} \rangle \left(\zeta_{14} \langle \hat{b}_{16\alpha}^\dagger \hat{b}_{14\alpha} \rangle^* + \zeta_{16} \langle \hat{b}_{16\alpha}^\dagger \hat{b}_{14\alpha} \rangle \right) \\ &\quad - ig_F \langle \hat{a} \rangle \left(1 + \langle \hat{b}_{14\alpha}^\dagger \hat{b}_{14\alpha} \rangle + \langle \hat{b}_{16\alpha}^\dagger \hat{b}_{16\alpha} \rangle \right) \end{aligned} \quad (\text{S48})$$

$$\begin{aligned} \frac{d}{dt} \langle \hat{b}_{16\alpha}^\dagger \hat{b}_{14\alpha} \rangle &= -((\gamma_{14} + \gamma_{16})/2 + i(\omega_{14} - \omega_{16})) \langle \hat{b}_{16\alpha}^\dagger \hat{b}_{14\alpha} \rangle - i\lambda \left(\langle \hat{b}_{16\alpha}^\dagger \hat{b}_{16\alpha} \rangle - \langle \hat{b}_{14\alpha}^\dagger \hat{b}_{14\alpha} \rangle \right) \\ &\quad - 2i\zeta_{14} \langle \hat{b}_{6\alpha} \rangle \langle \hat{b}_{16\alpha} \hat{b}_{14\alpha} \rangle^* + 2i\zeta_{16} \langle \hat{b}_{6\alpha} \rangle^* \langle \hat{b}_{16\alpha} \hat{b}_{14\alpha} \rangle \\ &\quad - ig_F \left(\langle \hat{a} \rangle \langle \hat{b}_{16\alpha} \hat{b}_{16\alpha} \rangle^* - \langle \hat{a} \rangle^* \langle \hat{b}_{14\alpha} \hat{b}_{14\alpha} \rangle \right). \end{aligned} \quad (\text{S49})$$

This system is supplemented with evolution equations for the complex conjugate variables $\langle \hat{O}_1 \hat{O}_2 \rangle^*$, which in principle do not contain additional information, but guarantee that diagonal occupation numbers (e.g., $\langle \hat{a}^\dagger \hat{a} \rangle$) are real and positive for all system parameters. The molecule index α runs over $\{1, 2, \dots, N\}$. To solve this system of equations, we first write it in the matrix form as

$$\frac{d}{dt} \mathbf{X} = \mathbf{M}(\mathbf{X}, \mathbf{X}^*) \cdot \mathbf{X}, \quad (\text{S50})$$

where $\mathbf{X} = [\langle \hat{a} \rangle, \langle \hat{a}^\dagger \hat{a} \rangle, \langle \hat{b}_{6,1} \rangle, \dots, \langle \hat{b}_{6,\alpha} \rangle, \dots]^T$ is high-dimensional vector whose components are the real-valued photon occupation variable ($\langle \hat{a}^\dagger \hat{a} \rangle$), the complex photon coherence ($\langle \hat{a} \rangle$), N cavity-vibration correlation variables ($\langle \hat{a} \hat{b}_{6\alpha} \rangle$), N complex vibrational coherences ($\langle \hat{b}_{6\alpha} \rangle$), $3N$ real-valued vibrational occupation numbers ($\nu_{6\alpha}, \nu_{14\alpha}, \nu_{16\alpha}$), and $4N$ complex vibration-vibration equal-time correlators (Fermi and bilinear couplings), giving the total vector dimension $D = 2 + 9N$. The elements of the D^2 -dimensional dynamical matrix $\mathbf{M}(\mathbf{X}, \mathbf{X}^*)$ have explicit dependence on the components of \mathbf{X} and its Hermitian conjugate \mathbf{X}^* due to the factorization scheme [see Eq. (S49)]. For moderate ensemble sizes $N < 10$, the propagation of the nonlinear equation from a suitable initial state $\mathbf{X}(0)$ is numerically tractable, and compares well with a brute-force propagation of the (linear) quantum master equation. However, for larger ensembles $N > 10$ we solve directly for the steady state \mathbf{X}_{ss} by setting time derivatives

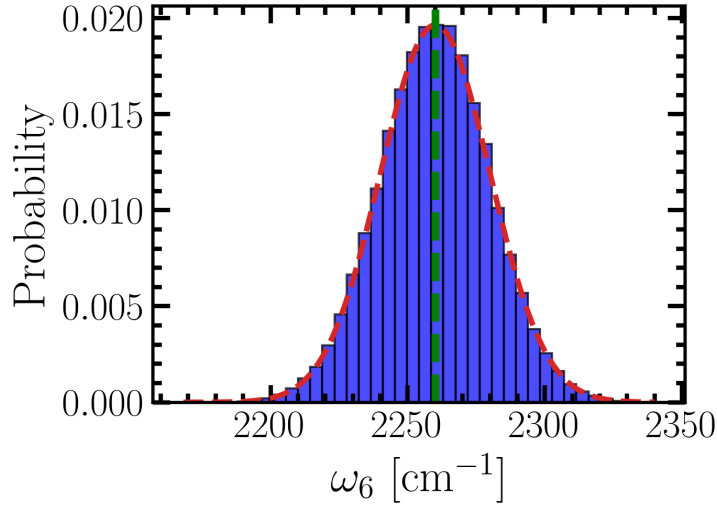


Figure S17: Normalized histogram of ν_6 fundamental vibration frequencies for an ensemble of $N = 300$ phenyl isocyanate (PHI) molecules. The histogram corresponds to 200 disorder realizations and the dashed line is a Gaussian fit of the histogram with extracted average $\bar{\omega}_6 = 2260.04 \text{ cm}^{-1}$ (dashed vertical line) and standard deviation $\sigma = 19.998 \text{ cm}^{-1}$.

to zero in Eq. (S50), and numerically solving the nonlinear root finding problem

$$\mathbf{M} \cdot \mathbf{X}_{ss} = 0 \quad (\text{S51})$$

6.4.2 Cavity-dependent vibrational occupations with energy disorder

As a minimal model for a inhomogenous intracavity molecular ensemble we consider the fundamental frequency of the PHI reactants ω_6 to be randomly distributed according to a Gaussian with an average frequency $\bar{\omega}_6 = 2260 \text{ cm}^{-1}$ and tunable standard deviation σ . By fitting the experimental cavity-free absorption spectrum in Fig. S11, we extract the value $\sigma = 20 \text{ cm}^{-1}$, which is comparable to the homogeneous linewidth γ_6 in Table S4. Other Hamiltonian and dissipator parameters are assumed to be homogeneously distributed in the ensemble. In Fig. S17, we show a ν_6 Gaussian frequency distribution that is representative for the calculations with an ensemble of $N = 300$ molecules. Similar frequency histograms are produced for other values of $N > 2$. To ensure good disorder statistics, we use a number of disorder configurations N_c that is comparable of larger than $\sim N$.

For fixed ensemble size N , we sample a disorder configuration $\{\omega_{6,1}, \dots, \omega_{6,\alpha} \dots \omega_{6,N}\}$ from a Gaussian distribution with average $\bar{\omega}_6 = 2260.0 \pm 0.1 \text{ cm}^{-1}$ and standard deviation $\sigma = 20.0 \pm 0.01 \text{ cm}^{-1}$, and use these frequencies as input to solve the nonlinear algebraic Eq. (S51) to obtain the steady state dynamical vector \mathbf{X}_{ss} , from which we extract the vibrational occupations of all the molecules in the ensemble $\langle \hat{b}_{6j}^\dagger \hat{b}_{6j} \rangle_{\text{ss}}$, for $j = 1, 2, \dots, N$. Other parameters of the evolution equations are fixed to the values used in Fig. S12, except for the single-molecule Rabi frequencies $g_{6,j}$. These local light-matter coupling parameters are chosen such that the Rabi splitting of the ensemble in linear transmission is $\Omega_N = 110 \text{ cm}^{-1}$, in close agreement with experiments. Assuming homogeneous couplings, we thus set $g_{6,j} = (55/\sqrt{N}) \text{ cm}^{-1}$.

In Fig. S18, we analyze the distribution of steady-state ν_6 vibrational occupation numbers $\langle \hat{b}_{6j}^\dagger \hat{b}_{6j} \rangle_{\text{ss}}$ for an ensemble of $N = 50$ PHI molecules, as a function of the cavity frequency ω_c . We include up to $N_c = 1000$ disorder configurations in the analysis to produce sufficient statistics. For reference, in Fig. S18a we reproduce the free-space vibrational absorption spectrum of PHI around the ν_6 resonance from Fig. S11. Figure S18b shows the most-probable value (mode) of the relative deviations $\Delta n_{6j}/n_6$ for different values of ω_c , demonstrating a resonant cooling feature at 2280 cm^{-1} , which is slightly blue-shifted relative to the free-space ν_6 resonance, in agreement with the intracavity rate measurements from the main text. The corresponding cavity-frequency dependence of the median of the $\Delta n_{6j}/n_6$ distribution is also given for comparison. The fact that these two measures of central tendency differ is a consequence of the asymmetric form of the distribution relative to the average. To better illustrate this point, in Figs. S18c, S18d, S18e, S18f, we show the histograms of the $\Delta n_{6j}/n_6$ steady-state distributions at 2200 cm^{-1} , 2280 cm^{-1} , 2350 cm^{-1} and 2600 cm^{-1} , respectively. In general, for all the cavity frequencies considered the $\Delta n_6/n_6$ distributions are asymmetric relative to the most probable value $\tilde{\Delta} n_6$ (mode). Specifically the distributions are right skewed, with the average $\bar{\Delta} n_6$ being higher than the median and the mode, for all the cavity frequencies studied. In Fig. S18b, we also show that including orientational average over the Rabi couplings

does not significantly change the frequency dependence of $\Delta n_6/n_6$. We include orientational disorder by averaging over a uniform distribution of dipole angles θ_i in the Rabi frequencies $g_i = g \cos(\theta_i)$, on top of the energy disorder distribution from Fig. S17.

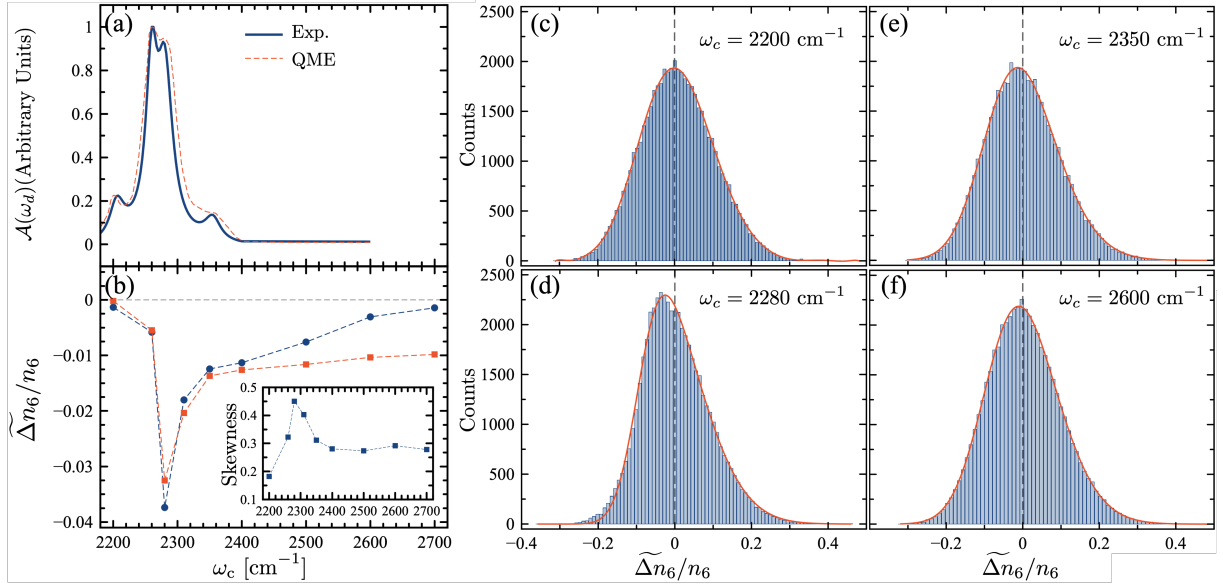


Figure S18: (a) Fitting of normalized absorption spectrum in the region of reactant mode ν_{NCO} (ν_6) located at 2260 cm⁻¹. Second peak at ~ 2280 cm⁻¹ corresponds to the combinational mode ν_{C} . (b) Mode of the deviations from the free-space thermal occupation at room temperature ($\Delta n_6/n_6$) for fundamental mode ν_6 at steady state as a function of cavity frequency ω_c . We consider $N = 50$ and 1000 configurations of disorder in the fundamental mode ν_6 with $\sigma = 20$ cm⁻¹. Squares (red line) corresponds to the case with orientational disorder. (c)-(f) Total distributions of occupation number at steady state for different cavity frequencies.

Finally, in Fig. S19, we show the scaling of the resonant cooling feature $\Delta n_6/n_6$ at 2280 cm⁻¹ as a function of the molecule number N , with all other system and reservoir parameters as in Fig. S18. For a given ensemble size, we obtain $\Delta n_6/n_6$ histograms with a sufficient number of disorder configurations N_c to obtain a reasonably converged fitted value for the mode $\tilde{\Delta}n_6$. For $N = 150$, we use $N_c > 1000$. The log-log plot in Fig. S19a confirms that for a homogeneous ensemble ($\sigma = 0$) we expect a $1/N$ scaling of the vibrational cooling feature on resonance. However, for finite values of σ , in general we expect the algebraic scaling $N^{-\alpha}$ of the mode, with $\alpha < 1$. In Fig. S19b, we numerically extract the dependence of the scaling

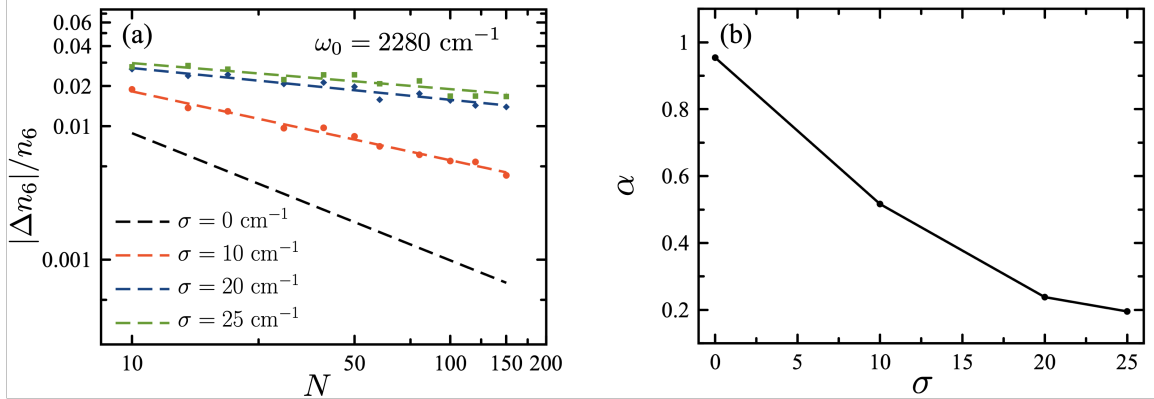


Figure S19: (a) Mode of the deviations from the free-space thermal occupation at room temperature $\Delta n_6/n_6$ at steady state as a function of number of molecules for different disorder distributions. (b) Exponent values α as a function of disorder σ , where $\Delta n_6/n_6(N) \propto 1/N^\alpha$. Plots represent the case with $\omega_c = 2280 \text{ cm}^{-1}$ and 600 configurations.

exponent α with the Gaussian disorder width σ , confirming the $\alpha = 1$ homogeneous limit when $\sigma \ll \gamma$ and suggesting an asymptotic scaling $\sigma \sim 0.1$ in the limit $\sigma/\gamma \gg 1$, where the cooling feature becomes only weakly dependent on the particle number. This asymptotic limit is challenging to address for the largest values of $N \sim 100$ due to statistical noise.

We can understand the scaling behavior of Fig. S19b by analogy with the size scaling of the delocalization length L_c in Frenkel exciton models with energy disorder: First, diagonal disorder introduces an effective coherence size N^* that can be much smaller than number of coupled molecules N , depending on the ratio between the disorder strength and the off-diagonal exciton coupling J between molecular monomers [64]; Second, it is known that for a given disorder strength σ , the exciton delocalization length L_c does not grow indefinitely as a number of coupled molecules N increase, but saturates to a finite value that again depends on the ratio σ/J [65]. Therefore, the thermodynamic limit $N \rightarrow \infty$ does not imply an infinite $1/N$ dilution of the excitonic wavefunction. We find numerical evidence of the same saturating behavior in Fig. S19b, although larger ensemble sizes are needed to confirm the trend. For molecular polariton models with disorder, the role of partial delocalization in the intracavity dynamics of internal molecular degrees of freedom is far from being fully understood [41, 42].

7 Comparison with Previous Models

For better context with the recent literature, we briefly compare our approach to cavity chemistry theory with recent works that address the same problem, without attempting to give a comprehensive review of the topic. For that, we refer the reader to Refs. [66, 67, 68].

We focus on adiabatic reactions that proceed through the infrequent passage of reactants to products via collisions in condensed phase, by overcoming an activation barrier. We assume that the cavity reaction rate can be written as in Eq. (S9), implying that the free-space reaction energetics (enthalpy of reaction and activation energy) are absorbed into the standard transition state theory (TST) rate k_{TST} , and the cavity-induced modifications are embedded in the transmission prefactor κ . The second assumption rests on previous theory on the factors that affect the transmission coefficient $\kappa(T)$ in generalized formulation of transition state theory (TST) that accounts for quantum effects such as tunneling or internal level redistributions over chemically relevant timescales [51].

A general theory for the transmission factor κ under vibrational strong coupling (VSC) has yet to be developed, but building on the physical intuition that the microscopic state-dependent reaction probability depends on the population of the internal levels of the reactants [52], we postulate the generic functional dependence $\kappa = \mathcal{F}(\Delta n_R/n_R^{\text{th}})$, where n_R^{th} is the average thermal occupation of the reactive vibrational coordinate and Δn_R is its deviation from thermal equilibrium. To lowest order in the ratio $z = \Delta n_R/n_R^{\text{th}}$, we expect the linear form $F(z) \approx 1 + \alpha z$, where α is some positive constant that has yet to be defined from first principles. Therefore, we expect an enhanced reactivity relative to free space for $z > 0$ and suppression for $z < 0$. Equilibrium TST rates should be expected inside the cavity if there are no deviations from the thermal Boltzmann vibrational distribution ($z = 0$), which is in agreement with the classical mechanics analysis from Ref. [69]. For the urethane formation reaction, we identify a specific reactive vibrational mode (ν_6 in PHI) and use an open quantum system model to compute $\Delta n_R/n_R^{\text{th}}$ for an ensemble of N molecules under VSC, as a function of the cavity resonance frequency and other experimentally-relevant cavity parameters. We take

into account the thermalization of vibrational and photonic degrees of freedom with a reservoir at 300 K. The equilibration of the cavity field with the thermal background radiation has been ignored in previous works, which have primarily addressed the role of photon decay in the intracavity vibrational dynamics [70, 71].

Static modifications of the vibrational observables such as the bond length or the nuclear excitation energy due to VSC were first studied in Ref. [72], using a fully quantum mechanical model of a single anharmonic molecule in a cavity. Specifically, the phenomenon of *bond strengthening* for resonant light-matter interaction was introduced and interpreted as the mixing of excited vibrational levels with low photon numbers with vibration-cavity dressed states that have a higher number of cavity photons but lower vibrational quantum numbers. The same idea was recently used to interpret a reduced vibrational mode occupations of a single reactant molecule evolving along a bimolecular reactive trajectory inside a cavity, relative to free space [40]. The nuclear and photon coordinates were treated classically using Ehrenfest dynamics and ab-initio electronic structure theory. Despite the limited number of reactive replicas and the short (sub-ps) simulation time, the idea that a cavity-frequency dependent redistribution of vibrational energy under VSC could be relevant in polaritonic chemistry is consistent with the quantum statistical mechanics treatment we developed. Vibrational energy redistributions over ps timescales were also found to explain the predicted rate modifications of unimolecular reaction under VSC [73], also for a single molecule in a cavity with classical nuclei and photons. In summary, these single molecule studies support the idea that a deviation of the internal vibrational level distribution is possible and is intimately related to the correlation between nuclear and photonic degrees of freedom established under VSC. In Sec. 6.2, we developed a simple model that explicitly connects the vibrational occupation of reactants with stationary light-matter coherence, for a single molecule in a multi-mode infrared resonator. The formalism can be further developed and compared numerical studies of realistic molecular systems. It remains to be fully understood whether engineering quantum mechanical light-matter correlations could lead to non-trivial chemical effects that cannot be captured with a

purely classical (mean field) correlations.

Many-particle studies of intracavity chemistry have shown that while rate modifications due to VSC could be possible with homogeneous ensembles for very specific regimes of non-adiabatic electron transfer reactions [74], in general it is understood that due to many-body dilution of the vibrational excited state wavefunctions, the influence of cavity photons on reduced vibrational state of individual molecules is monotonically reduced with increasing molecule number N [73, 75]. This seems to be a general feature of the problem that could also be formulated in purely incoherent statistical terms as a mismatch between densities of states of low-energy excitations with different photon content [76]. In this work (Sec. 6.4.2), we confirm many-body dilution for homogeneous ensembles, but offer new insights on how energy disorder can protect stationary light-matter coherences in VSC from the detrimental effect of wavefunction delocalization. We find statistical deviations of the vibrational distribution relative to a thermal Boltzmann despite the large density of states mismatch between states with high and low photon content, suggesting that statistical approaches that ignore correlations between photonic and vibrational degrees of freedom, such as Ref. [76], may only partially describe the physics of the problem. One way to generalize the theoretical study of cavity chemistry could follow the approach of Ref. [50], where a quantum TST formulation is used to predict cavity-induced modifications of the polaritonic partition function under VSC. Although the rate modifications in Ref. [50] are attributed to global spectral changes of the coupled system, not to internal level populations of reactants or products, formulating the rate theory quantum mechanically would enable the analysis of non-canonical molecular statistics [38] that could possibly emerge when photonic degrees of freedom are traced out from a thermal polaritonic density matrix. The approach would also serve as a tool for developing the theory that connects the vibrational population deviations $\Delta n_R/n_R^{\text{th}}$ discussed in this work, with the rate constant k for bimolecular reactions in infrared cavities, as the quantum mechanically approach performed in Ref. [77] in the context of left-to-right transmission rates of a double-well potential for $N = 1$, where the cavity mode couples directly both reactant and product states, and considering

the influence of structured environments and solvent friction.

References and Notes

1. A. H. Zewail, Laser selective chemistry—Is it possible? *Phys. Today* **33**, 27–33 (1980). [doi:10.1063/1.2913821](https://doi.org/10.1063/1.2913821)
2. W. S. Warren, H. Rabitz, M. Dahleh, Coherent control of quantum dynamics: The dream is alive. *Science* **259**, 1581–1589 (1993). [doi:10.1126/science.259.5101.1581](https://doi.org/10.1126/science.259.5101.1581) [Medline](#)
3. T. Stensitzki, Y. Yang, V. Kozich, A. A. Ahmed, F. Kössl, O. Kühn, K. Heyne, Acceleration of a ground-state reaction by selective femtosecond-infrared-laser-pulse excitation. *Nat. Chem.* **10**, 126–131 (2018). [doi:10.1038/nchem.2909](https://doi.org/10.1038/nchem.2909) [Medline](#)
4. M. Delor, P. A. Scattergood, I. V. Sazanovich, A. W. Parker, G. M. Greetham, A. J. H. M. Meijer, M. Towrie, J. A. Weinstein, Toward control of electron transfer in donor-acceptor molecules by bond-specific infrared excitation. *Science* **346**, 1492–1495 (2014). [doi:10.1126/science.1259995](https://doi.org/10.1126/science.1259995) [Medline](#)
5. Z. Lin, C. M. Lawrence, D. Xiao, V. V. Kireev, S. S. Skourtis, J. L. Sessler, D. N. Beratan, I. V. Rubtsov, Modulating unimolecular charge transfer by exciting bridge vibrations. *J. Am. Chem. Soc.* **131**, 18060–18062 (2009). [doi:10.1021/ja907041t](https://doi.org/10.1021/ja907041t) [Medline](#)
6. A. Assion, T. Baumert, M. Bergt, T. Brixner, B. Kiefer, V. Seyfried, M. Strehle, G. Gerber, Control of chemical reactions by feedback-optimized phase-shaped femtosecond laser pulses. *Science* **282**, 919–922 (1998). [doi:10.1126/science.282.5390.919](https://doi.org/10.1126/science.282.5390.919) [Medline](#)
7. M. P. A. Branderhorst, P. Londero, P. Wasylczyk, C. Brif, R. L. Kosut, H. Rabitz, I. A. Walmsley, Coherent control of decoherence. *Science* **320**, 638–643 (2008). [doi:10.1126/science.1154576](https://doi.org/10.1126/science.1154576) [Medline](#)
8. A. Thomas, J. George, A. Shalabney, M. Dryzhakov, S. J. Varma, J. Moran, T. Chervy, X. Zhong, E. Devaux, C. Genet, J. A. Hutchison, T. W. Ebbesen, Ground-state chemical reactivity under vibrational coupling to the vacuum electromagnetic field. *Angew. Chem. Int. Ed.* **55**, 11462–11466 (2016). [doi:10.1002/anie.201605504](https://doi.org/10.1002/anie.201605504) [Medline](#)
9. A. Thomas, L. Lethuillier-Karl, K. Nagarajan, R. M. A. Vergauwe, J. George, T. Chervy, A. Shalabney, E. Devaux, C. Genet, J. Moran, T. W. Ebbesen, Tilting a ground-state reactivity landscape by vibrational strong coupling. *Science* **363**, 615–619 (2019). [doi:10.1126/science.aau7742](https://doi.org/10.1126/science.aau7742) [Medline](#)
10. F. J. Garcia-Vidal, C. Ciuti, T. W. Ebbesen, Manipulating matter by strong coupling to vacuum fields. *Science* **373**, eabd0336 (2021). [doi:10.1126/science.abd0336](https://doi.org/10.1126/science.abd0336) [Medline](#)
11. B. S. Simpkins, A. D. Dunkelberger, J. C. Owrtusky, Mode-specific chemistry through vibrational strong coupling (or *a wish come true*). *J. Phys. Chem. C* **125**, 19081–19087 (2021). [doi:10.1021/acs.jpcc.1c05362](https://doi.org/10.1021/acs.jpcc.1c05362)
12. F. Herrera, J. Owrtusky, Molecular polaritons for controlling chemistry with quantum optics. *J. Chem. Phys.* **152**, 100902 (2020). [doi:10.1063/1.5136320](https://doi.org/10.1063/1.5136320) [Medline](#)
13. G. Khitrova, H. M. Gibbs, M. Kira, S. W. Koch, A. Scherer, Vacuum Rabi splitting in semiconductors. *Nat. Phys.* **2**, 81–90 (2006). [doi:10.1038/nphys227](https://doi.org/10.1038/nphys227)
14. J. P. Long, B. S. Simpkins, Coherent coupling between a molecular vibration and Fabry–Perot optical cavity to give hybridized states in the strong coupling limit. *ACS Photonics* **2**, 130–136 (2015). [doi:10.1021/ph5003347](https://doi.org/10.1021/ph5003347)

15. A. Shalabney, J. George, J. Hutchison, G. Pupillo, C. Genet, T. W. Ebbesen, Coherent coupling of molecular resonators with a microcavity mode. *Nat. Commun.* **6**, 5981 (2015). [doi:10.1038/ncomms6981](https://doi.org/10.1038/ncomms6981) [Medline](#)
16. J. Del Pino, J. Feist, F. J. Garcia-Vidal, Quantum theory of collective strong coupling of molecular vibrations with a microcavity mode. *New J. Phys.* **17**, 053040 (2015). [doi:10.1088/1367-2630/17/5/053040](https://doi.org/10.1088/1367-2630/17/5/053040)
17. J. A. Hutchison, T. Schwartz, C. Genet, E. Devaux, T. W. Ebbesen, Modifying chemical landscapes by coupling to vacuum fields. *Angew. Chem. Int. Ed.* **51**, 1592–1596 (2012). [doi:10.1002/anie.201107033](https://doi.org/10.1002/anie.201107033) [Medline](#)
18. B. Munkhbat, M. Wersäll, D. G. Baranov, T. J. Antosiewicz, T. Shegai, Suppression of photo-oxidation of organic chromophores by strong coupling to plasmonic nanoantennas. *Sci. Adv.* **4**, eaas9552 (2018). [doi:10.1126/sciadv.aas9552](https://doi.org/10.1126/sciadv.aas9552) [Medline](#)
19. J. Lather, P. Bhatt, A. Thomas, T. W. Ebbesen, J. George, Cavity catalysis by cooperative vibrational strong coupling of reactant and solvent molecules. *Angew. Chem. Int. Ed.* **58**, 10635–10638 (2019). [doi:10.1002/anie.201905407](https://doi.org/10.1002/anie.201905407) [Medline](#)
20. B. S. Simpkins, K. P. Fears, W. J. Dressick, B. T. Spann, A. D. Dunkelberger, J. C. Owrtusky, Spanning strong to weak normal mode coupling between vibrational and Fabry–Pérot cavity modes through tuning of vibrational absorption strength. *ACS Photonics* **2**, 1460–1467 (2015). [doi:10.1021/acspophotonics.5b00324](https://doi.org/10.1021/acspophotonics.5b00324)
21. C. Weisbuch, M. Nishioka, A. Ishikawa, Y. Arakawa, Observation of the coupled exciton–photon mode splitting in a semiconductor quantum microcavity. *Phys. Rev. Lett.* **69**, 3314–3317 (1992). [doi:10.1103/PhysRevLett.69.3314](https://doi.org/10.1103/PhysRevLett.69.3314) [Medline](#)
22. W. Ahn, I. Vurgaftman, A. D. Dunkelberger, J. C. Owrtusky, B. S. Simpkins, Vibrational strong coupling controlled by spatial distribution of molecules within the optical cavity. *ACS Photonics* **5**, 158–166 (2018). [doi:10.1021/acspophotonics.7b00583](https://doi.org/10.1021/acspophotonics.7b00583)
23. S. Wang, T. Chervy, J. George, J. A. Hutchison, C. Genet, T. W. Ebbesen, Quantum yield of polariton emission from hybrid light-matter states. *J. Phys. Chem. Lett.* **5**, 1433–1439 (2014). [doi:10.1021/jz5004439](https://doi.org/10.1021/jz5004439) [Medline](#)
24. A. D. Dunkelberger, A. B. Grafton, I. Vurgaftman, O. O. Soyal, T. L. Reinecke, R. B. Davidson II, B. S. Simpkins, J. C. Owrtusky, Saturable absorption in solution-phase and cavity-coupled tungsten hexacarbonyl. *ACS Photonics* **6**, 2719–2725 (2019). [doi:10.1021/acspophotonics.9b00703](https://doi.org/10.1021/acspophotonics.9b00703)
25. R. Houdré, J. L. Gibernon, P. Pellandini, R. P. Stanley, U. Oesterle, C. Weisbuch, J. O’Gorman, B. Roycroft, M. Illegems, Saturation of the strong-coupling regime in a semiconductor microcavity: Free-carrier bleaching of cavity polaritons. *Phys. Rev. B* **52**, 7810–7813 (1995). [doi:10.1103/PhysRevB.52.7810](https://doi.org/10.1103/PhysRevB.52.7810) [Medline](#)
26. J. J. Pietron, K. P. Fears, J. C. Owrtusky, B. S. Simpkins, Electrochemical modulation of strong vibration–cavity coupling. *ACS Photonics* **7**, 165–173 (2020). [doi:10.1021/acspophotonics.9b01339](https://doi.org/10.1021/acspophotonics.9b01339)
27. W. Ahn, B. S. Simpkins, Spectroelectrochemical measurement and modulation of exciton–polaritons. *APL Photonics* **5**, 076107 (2020). [doi:10.1063/5.0012528](https://doi.org/10.1063/5.0012528)

28. M. V. Imperatore, J. B. Asbury, N. C. Giebink, Reproducibility of cavity-enhanced chemical reaction rates in the vibrational strong coupling regime. *J. Chem. Phys.* **154**, 191103 (2021). [Medline](#)
29. G. D. Wiesehan, W. Xiong, Negligible rate enhancement from reported cooperative vibrational strong coupling catalysis. *J. Chem. Phys.* **155**, 241103 (2021). [doi:10.1063/5.0077549](https://doi.org/10.1063/5.0077549) [Medline](#)
30. E. Delebecq, J.-P. Pascault, B. Boutevin, F. Ganachaud, On the versatility of urethane/urea bonds: Reversibility, blocked isocyanate, and non-isocyanate polyurethane. *Chem. Rev.* **113**, 80–118 (2013). [doi:10.1021/cr300195n](https://doi.org/10.1021/cr300195n) [Medline](#)
31. F. Kössl, M. Lisaj, V. Kozich, K. Heyne, O. Kühn, Monitoring the alcoholysis of isocyanates with infrared spectroscopy. *Chem. Phys. Lett.* **621**, 41–45 (2015). [doi:10.1016/j.cplett.2014.12.042](https://doi.org/10.1016/j.cplett.2014.12.042)
32. G. Raspoet, M. T. Nguyen, M. McGarragh, A. F. Hegarty, The alcoholysis reaction of isocyanates giving urethanes: Evidence for a multimolecular mechanism. *J. Org. Chem.* **63**, 6878–6885 (1998). [doi:10.1021/jo9806411](https://doi.org/10.1021/jo9806411) [Medline](#)
33. A. A. Caraculacu, S. Coseri, Isocyanates in polyaddition processes. Structure and reaction mechanisms. *Prog. Polym. Sci.* **26**, 799–851 (2001). [doi:10.1016/S0079-6700\(00\)00033-2](https://doi.org/10.1016/S0079-6700(00)00033-2)
34. M. Çoban, F. A. S. Konuklar, A computational study on the mechanism and the kinetics of urethane formation. *Comput. Theor. Chem.* **963**, 168–175 (2011). [doi:10.1016/j.comptc.2010.10.017](https://doi.org/10.1016/j.comptc.2010.10.017)
35. K. J. Laidler, *Chemical Kinetics* (Pearson Education Inc., 1987).
36. C. Schäfer, M. Ruggenthaler, A. Rubio, *Ab initio* nonrelativistic quantum electrodynamics: Bridging quantum chemistry and quantum optics from weak to strong coupling. *Phys. Rev. A* **98**, 043801 (2018). [doi:10.1103/PhysRevA.98.043801](https://doi.org/10.1103/PhysRevA.98.043801)
37. M. Seidel, T. Chervy, A. Thomas, E. Akiki, R. M. A. Vergauwe, A. Shalabney, J. George, E. Devaux, J. A. Hutchison, C. Genet, T. W. Ebbesen, Correction to vibro-polaritonic IR emission in the strong coupling regime. *ACS Photonics* **6**, 1823–1825 (2019). [doi:10.1021/acspophotonics.8b01756](https://doi.org/10.1021/acspophotonics.8b01756)
38. D. Xu, J. Cao, Non-canonical distribution and non-equilibrium transport beyond weak system-bath coupling regime: A polaron transformation approach. *Front. Phys. (Beijing)* **11**, 110308 (2016). [doi:10.1007/s11467-016-0540-2](https://doi.org/10.1007/s11467-016-0540-2)
39. T. E. Li, J. E. Subotnik, A. Nitzan, Cavity molecular dynamics simulations of liquid water under vibrational ultrastrong coupling. *Proc. Natl. Acad. Sci. U.S.A.* **117**, 18324–18331 (2020). [doi:10.1073/pnas.2009272117](https://doi.org/10.1073/pnas.2009272117) [Medline](#)
40. C. Schäfer, J. Flick, E. Ronca, P. Narang, A. Rubio, Shining light on the microscopic resonant mechanism responsible for cavity-mediated chemical reactivity. *Nat. Commun.* **13**, 7817 (2022). [doi:10.1038/s41467-022-35363-6](https://doi.org/10.1038/s41467-022-35363-6) [Medline](#)
41. D. Wellnitz, G. Pupillo, J. Schachenmayer, Disorder enhanced vibrational entanglement and dynamics in polaritonic chemistry. *Commun. Phys.* **5**, 120 (2022). [doi:10.1038/s42005-022-00892-5](https://doi.org/10.1038/s42005-022-00892-5)

42. M. Du, J. Yuen-Zhou, Catalysis by dark states in vibropolaritonic chemistry. *Phys. Rev. Lett.* **128**, 096001 (2022). [doi:10.1103/PhysRevLett.128.096001](https://doi.org/10.1103/PhysRevLett.128.096001) [Medline](#)
43. J. F. Triana, F. Recabal, F. Herrera, B. S. Simpkins, W. Ahn, Data: Modification of ground state chemical reactivity via light-matter coherence in infrared cavities, version 2, Zenodo (2023); <https://doi.org/10.5281/zenodo.7915873>.
44. M. Born, E. Wolf, *Principles of Optics: Electromagnetic Theory of Propagation, Interference and Diffraction of Light* (Elsevier, 2013)
45. H. J. Werner, P. J. Knowles, P. Celani, W. Györffy, A. Hesselmann, D. Kats, G. Knizia, A. Köhn, T. Korona, D. Kreplin, R. Lindh, Q. Ma, F. R. Manby, A. Mitrushenkov, G. Rauhut, M. Schütz, K. R. Shamasundar, T. B. Adler, R. D. Amos, S. J. Bennie, A. Bernhardsson, A. Berning, J. A. Black, P. J. Bygrave, R. Cimiraglia, D. L. Cooper, D. Coughtrie, M. J. O. Deegan, A. J. Dobbyn, K. Doll, M. Dornbach, F. Eckert, S. Erfort, E. Goll, C. Hampel, G. Hetzer, J. G. Hill, M. Hodges, T. Hrenar, G. Jansen, C. Köppl, C. Kollmar, S. J. R. Lee, Y. Liu, A. W. Lloyd, R. A. Mata, A. J. May, B. Mussard, S. J. McNicholas, W. Meyer, T. F. Miller III, M. E. Mura, A. Nicklass, D. P. O'Neill, P. Palmieri, D. Peng, K. A. Peterson, K. Pflüger, R. Pitzer, I. Polyak, M. Reiher, J. O. Richardson, J. B. Robinson, B. Schröder, M. Schwilk, T. Shiozaki, M. Sibaev, H. Stoll, A. J. Stone, R. Tarroni, T. Thorsteinsson, J. Toulouse, M. Wang, M. Welborn, B. Ziegler, MOLPRO, version 2018, a package of ab initio programs (2018); <https://www.molpro.net>.
46. N. S. Bayliss, E. G. McRae, Solvent effects in the spectra of acetone, crotonaldehyde, nitromethane and nitrobenzene. *J. Phys. Chem.* **58**, 1006–1011 (1954). [doi:10.1021/j150521a018](https://doi.org/10.1021/j150521a018)
47. G. W. Chantry, E. A. Nicol, D. J. Harrison, A. Bouchy, G. Roussy, Vibrational spectrum, assignment and molecular symmetry of phenyl isocyanate in the liquid phase. *Spectrochim. Acta A* **30**, 1717–1722 (1974). [doi:10.1016/0584-8539\(74\)80122-4](https://doi.org/10.1016/0584-8539(74)80122-4)
48. F. Billes, H. Böhlig, M. Ackermann, M. Kudra, A vibrational spectroscopic study on furan and its hydrated derivatives. *J. Mol. Struct. THEOCHEM* **672**, 1–16 (2004). [doi:10.1016/j.theochem.2003.10.067](https://doi.org/10.1016/j.theochem.2003.10.067)
49. S. Mukamel, *Principles of Nonlinear Optical Spectroscopy*, Oxford Series in Optical and Imaging Sciences (Oxford Univ. Press, 1995).
50. P.-Y. Yang, J. Cao, Quantum effects in chemical reactions under polaritonic vibrational strong coupling. *J. Phys. Chem. Lett.* **12**, 9531–9538 (2021). [doi:10.1021/acs.jpclett.1c02210](https://doi.org/10.1021/acs.jpclett.1c02210) [Medline](#)
51. X. Li, A. Mandal, P. Huo, Cavity frequency-dependent theory for vibrational polariton chemistry. *Nat. Commun.* **12**, 1315 (2021). [doi:10.1038/s41467-021-21610-9](https://doi.org/10.1038/s41467-021-21610-9) [Medline](#)
52. A. Fernández-Ramos, J. A. Miller, S. J. Klippenstein, D. G. Truhlar, Modeling the kinetics of bimolecular reactions. *Chem. Rev.* **106**, 4518–4584 (2006). [doi:10.1021/cr050205w](https://doi.org/10.1021/cr050205w) [Medline](#)
53. B. Widom, Reaction kinetics in stochastic models. *J. Chem. Phys.* **55**, 44–52 (1971). [doi:10.1063/1.1675541](https://doi.org/10.1063/1.1675541)

54. C. Lim, D. G. Truhlar, Internal-state nonequilibrium effects for a fast, second-order reaction. *J. Phys. Chem.* **89**, 5–7 (1985). [doi:10.1021/j100247a003](https://doi.org/10.1021/j100247a003)
55. C. Lim, D. G. Truhlar, New techniques for the study of non-equilibrium effects in non-first-order systems. *Chem. Phys. Lett.* **114**, 253–257 (1985). [doi:10.1016/0009-2614\(85\)80907-6](https://doi.org/10.1016/0009-2614(85)80907-6)
56. A. B. Grafton, A. D. Dunkelberger, B. S. Simpkins, J. F. Triana, F. J. Hernández, F. Herrera, J. C. Owrusky, Excited-state vibration-polariton transitions and dynamics in nitroprusside. *Nat. Commun.* **12**, 214 (2021). [doi:10.1038/s41467-020-20535-z](https://doi.org/10.1038/s41467-020-20535-z) [Medline](#)
57. H. Tanji-Suzuki, I. D. Leroux, M. H. Schleier-Smith, M. Cetina, A. T. Grier, J. Simon, V. Vuletic, “Chapter 4 - interaction between atomic ensembles and optical resonators: Classical description” in *Advances in Atomic, Molecular, and Optical Physics, Volume 60*, E. Arimondo, P. R. Berman, C. C. Lin, Eds. (Academic Press, 2011), pp. 201–237.
58. B. Zhu, J. Schachenmayer, M. Xu, F. Herrera, J. G. Restrepo, M. J. Holland, A. M. Rey, Synchronization of interacting quantum dipoles. *New J. Phys.* **17**, 083063 (2015). [doi:10.1088/1367-2630/17/8/083063](https://doi.org/10.1088/1367-2630/17/8/083063)
59. T. V. Tscherbul, P. Brumer, Non-equilibrium stationary coherences in photosynthetic energy transfer under weak-field incoherent illumination. *J. Chem. Phys.* **148**, 124114 (2018). [doi:10.1063/1.5028121](https://doi.org/10.1063/1.5028121) [Medline](#)
60. H. P. Breuer, F. Petruccione, S. P. A. P. F. Petruccione, *The Theory of Open Quantum Systems* (Oxford Univ. Press, 2002).
61. G. Alvarado Barrios, F. Albarrán-Arriagada, F. A. Cárdenas-López, G. Romero, J. C. Retamal, Role of quantum correlations in light-matter quantum heat engines. *Phys. Rev. A* **96**, 052119 (2017). [doi:10.1103/PhysRevA.96.052119](https://doi.org/10.1103/PhysRevA.96.052119)
62. N. Shammah, N. Lambert, F. Nori, S. De Liberato, Superradiance with local phase-breaking effects. *Phys. Rev. A* **96**, 023863 (2017). [doi:10.1103/PhysRevA.96.023863](https://doi.org/10.1103/PhysRevA.96.023863)
63. F. Herrera, F. C. Spano, Absorption and photoluminescence in organic cavity QED. *Phys. Rev. A* **95**, 053867 (2017). [doi:10.1103/PhysRevA.95.053867](https://doi.org/10.1103/PhysRevA.95.053867)
64. T. Meier, Y. Zhao, V. Chernyak, S. Mukamel, Polarons, localization, and excitonic coherence in superradiance of biological antenna complexes. *J. Chem. Phys.* **107**, 3876–3893 (1997). [doi:10.1063/1.474746](https://doi.org/10.1063/1.474746)
65. G. D. Scholes, Limits of exciton delocalization in molecular aggregates. *Faraday Discuss.* **221**, 265–280 (2019). [doi:10.1039/C9FD00064J](https://doi.org/10.1039/C9FD00064J) [Medline](#)
66. D. S. Wang, S. F. Yelin, A roadmap toward the theory of vibrational polariton chemistry. *ACS Photonics* **8**, 2818–2826 (2021). [doi:10.1021/acsphotonics.1c01028](https://doi.org/10.1021/acsphotonics.1c01028)
67. A. Mandal, M. Taylor, B. Weight, E. Koessler, X. Li, P. Huo, Theoretical advances in polariton chemistry and molecular cavity quantum electrodynamics. *ChemRxiv* 2022-g9lr7 [Preprint] (2022). <https://doi.org/10.26434/chemrxiv-2022-g9lr7>.
68. M. Sánchez-Barquilla, A. I. Fernández-Domínguez, J. Feist, F. J. García-Vidal, A theoretical perspective on molecular polaritonics. *ACS Photonics* **9**, 1830–1841 (2022). [doi:10.1021/acsphotonics.2c00048](https://doi.org/10.1021/acsphotonics.2c00048) [Medline](#)

69. T. E. Li, A. Nitzan, J. E. Subotnik, On the origin of ground-state vacuum-field catalysis: Equilibrium consideration. *J. Chem. Phys.* **152**, 234107 (2020). [doi:10.1063/5.0006472](https://doi.org/10.1063/5.0006472) [Medline](#)
70. M. Du, J. A. Campos-Gonzalez-Angulo, J. Yuen-Zhou, Nonequilibrium effects of cavity leakage and vibrational dissipation in thermally activated polariton chemistry. *J. Chem. Phys.* **154**, 084108 (2021). [doi:10.1063/5.0037905](https://doi.org/10.1063/5.0037905) [Medline](#)
71. J. F. Triana, M. Arias, J. Nishida, E. A. Muller, R. Wilcken, S. C. Johnson, A. Delgado, M. B. Raschke, F. Herrera, Semi-empirical quantum optics for mid-infrared molecular nanophotonics. *J. Chem. Phys.* **156**, 124110 (2022). [doi:10.1063/5.0075894](https://doi.org/10.1063/5.0075894) [Medline](#)
72. F. J. Hernández, F. Herrera, Multi-level quantum Rabi model for anharmonic vibrational polaritons. *J. Chem. Phys.* **151**, 144116 (2019). [doi:10.1063/1.5121426](https://doi.org/10.1063/1.5121426) [Medline](#)
73. J. Sun, O. Vendrell, Suppression and enhancement of thermal chemical rates in a cavity. *J. Phys. Chem. Lett.* **13**, 4441–4446 (2022). [doi:10.1021/acs.jpclett.2c00974](https://doi.org/10.1021/acs.jpclett.2c00974) [Medline](#)
74. J. A. Campos-Gonzalez-Angulo, R. F. Ribeiro, J. Yuen-Zhou, Resonant catalysis of thermally activated chemical reactions with vibrational polaritons. *Nat. Commun.* **10**, 4685 (2019). [doi:10.1038/s41467-019-12636-1](https://doi.org/10.1038/s41467-019-12636-1) [Medline](#)
75. A. Mandal, X. Li, P. Huo, Theory of vibrational polariton chemistry in the collective coupling regime. *J. Chem. Phys.* **156**, 014101 (2022). [doi:10.1063/5.0074106](https://doi.org/10.1063/5.0074106) [Medline](#)
76. I. Vurgaftman, B. S. Simpkins, A. D. Dunkelberger, J. C. Owrtsky, Negligible effect of vibrational polaritons on chemical reaction rates via the density of states pathway. *J. Phys. Chem. Lett.* **11**, 3557–3562 (2020). [doi:10.1021/acs.jpclett.0c00841](https://doi.org/10.1021/acs.jpclett.0c00841) [Medline](#)
77. L. P. Lindoy, A. Mandal, D. R. Reichman, Quantum dynamics of vibrational polariton chemistry. [arXiv:2210.05550](https://arxiv.org/abs/2210.05550) [quant-ph] (2022).